

2020-01-01

SynThesis and Advanced Manufacturing of Polymer Structures and Their Composites

Bethany Rose Wilburn
University of Texas at El Paso

Follow this and additional works at: https://scholarworks.utep.edu/open_etd



Part of the [Mechanical Engineering Commons](#)

Recommended Citation

Wilburn, Bethany Rose, "SynThesis and Advanced Manufacturing of Polymer Structures and Their Composites" (2020). *Open Access Theses & Dissertations*. 3060.
https://scholarworks.utep.edu/open_etd/3060

This is brought to you for free and open access by ScholarWorks@UTEP. It has been accepted for inclusion in Open Access Theses & Dissertations by an authorized administrator of ScholarWorks@UTEP. For more information, please contact lweber@utep.edu.

SYNTHESIS AND ADVANCED MANUFACTURING OF POLYMER STRUCTURES AND
THEIR COMPOSITES

BETHANY ROSE WILBURN

Master's Program in Mechanical Engineering

APPROVED:

Yirong Lin, Ph.D., Chair

Thomas Robison, Ph.D., co-Chair

Tzu-Liang (Bill) Tseng, Ph.D.

Stephen L. Crites, Jr., Ph.D.
Dean of the Graduate School

Copyright ©

by

Bethany R. Wilburn

2020

Dedication

Thank you for your constant support, love, and care.

*To my family, Carmen, John, Camille, Heather; to my girlfriend, Elizabeth; and to my friends,
The Series.*

SYNTHESIS AND ADVANCED MANUFACTURING OF POLYMER STRUCTURES AND
THEIR COMPOSITES

by

BETHANY ROSE WILBURN, B.S.

THESIS

Presented to the Faculty of the Graduate School of

The University of Texas at El Paso

in Partial Fulfillment

of the Requirements

for the Degree of

MASTER OF SCIENCE

Department of Mechanical Engineering

THE UNIVERSITY OF TEXAS AT EL PASO

May 2020

Acknowledgements

First and foremost, I would like to thank Dr. Yirong Lin for all support, generosity, and guidance he gave me for these past four years. Dr. Lin provided me with the necessary tools and opportunities that have notably helped shape my career. It was a great honor to be taught not only how to conduct research and advance my professional development by your mentorship, but also life lessons and how to be a great leader. I would also like to give a special thanks to Dr. Robison for proving great advice regarding my research project and for serving on my committee. Also, thank you to Sabrina for your guidance and constant support throughout this research. I would also like to thank Dr. Tseng for not only serving on my committee, but for your generosity.

Thank you to all my lab mates for your continuous support and teachings; specifically thank you to Luis, Delfin, Hilda, Sam, Jaime, and Anabel. Thank you to Frank, Mariana, and Nik for the close friendships we formed from the beginning of our college career where we spent many late library nights working together to help each other succeed. I would also like give my sincerest thanks to the love and encouragement from my parents, my sister, my niece, my girlfriend, and my closest friends; you all have been the foundation of my drive and motivation throughout all that I pursue.

Lastly, thank you to the various programs and facilities that provided their support throughout my undergraduate and graduate careers: DOE, NSF-PREM, COURI, KCNSC, cSETR, and Keck Center. I would like to give a distinct thank you to The University of Texas at El Paso and the Mechanical Engineering Department for allowing me the opportunity to conduct my research.

Table of Contents

| | |
|--|------|
| Acknowledgements..... | v |
| Table of Contents..... | vi |
| List of Tables..... | viii |
| List of Figures..... | ix |
| Chapter 1: Introduction..... | 1 |
| Chapter 2: Dispersion Polymerization of Hollow Polysiloxane Microspheres Using Templated Polystyrene Core..... | 3 |
| 2.1 Introduction and Background..... | 3 |
| 2.1.1 Scope of Project..... | 4 |
| 2.1.2 Dispersion Polymerization..... | 5 |
| 2.2 Chemical Synthesis..... | 5 |
| 2.2.1 Experimental Materials..... | 6 |
| 2.2.2 Formation of Core..... | 6 |
| 2.2.3 Mechanism for Free-Radical Initiation of Polystyrene..... | 7 |
| 2.2.4 Factors Contributing to Particle Size of Templated Core..... | 8 |
| 2.2.5 Hydrolysis and Condensation of MTMS..... | 8 |
| 2.3 Results..... | 9 |
| 2.3.1 Growth of Templated Particles..... | 9 |
| 2.3.2 Crosslinking of Polysiloxane Shell..... | 19 |
| 2.3.3 Calcination of Hollow Polysiloxane Microspheres..... | 22 |
| 2.3.4 Additive Manufacturing of Pore Formers..... | 25 |
| 2.4 Conclusion..... | 27 |
| Chapter 3: Additive Manufacturing of Polyetheretherketone for High Temperature Applications..... | 29 |
| 3.1 Introduction..... | 29 |
| 3.1.1 Additive Manufacturing of PEEK..... | 30 |
| 3.1.2 Crystallinity..... | 31 |
| 3.1.3 Thermal Post-Processing..... | 31 |
| 3.2 Results..... | 33 |
| 3.2.1 Mechanical Testing..... | 33 |

| | | |
|-----------------|---|----|
| 3.2.2 | Degree of Crystallinity..... | 35 |
| 3.2.3 | Sulfonation..... | 38 |
| 3.3 | Conclusion | 40 |
| Chapter 4: | Multifunctional Sensing Using 3D Printed CNTs/BTO/PVDF Nanocomposites | 42 |
| 4.1 | Introduction and Background | 42 |
| 4.2 | Motivation of FDM Printing Multifunctional Sensors | 43 |
| 4.3 | Methodology | 44 |
| 4.3.1 | Additive Manufacturing of Nanocomposites..... | 45 |
| 4.3.2 | Characterization..... | 45 |
| 4.3.3 | Multifunctional Testing..... | 46 |
| 4.4 | Results..... | 47 |
| 4.4.1 | Multifunctional Property Testing: Temperature Sensing | 47 |
| 4.4.2 | Multifunctional Property Testing: Stress-Strain..... | 49 |
| 4.5 | Conclusion | 51 |
| Chapter 5: | Summary of Research and Future Work..... | 53 |
| 5.1 | Conclusions..... | 53 |
| 5.2 | Recommendations for Future Work..... | 55 |
| References..... | | 58 |
| Vita..... | | 67 |

List of Tables

| | |
|---|----|
| Table 2.1 Effect of temperature and feeding rate on PS core microspheres..... | 12 |
| Table 3.1 Intamsys Funmat HT FDM printing parameters of PEEK..... | 31 |

List of Figures

| | |
|---|----|
| Figure 2.1. Applications of hollow microspheres materials | 4 |
| Figure 2.2. Experimental setup for dispersion polymerization of polystyrene..... | 7 |
| Figure 2.3. Depiction of radical initiation of BPO for the addition polymerization of styrene..... | 8 |
| Figure 2.4. SEM images of polystyrene core microspheres with the corresponding reactants from Table 2.1 | 14 |
| Figure 2.5. Effect of temperature on the average diameter and coefficient of variation of the templated polystyrene microspheres | 15 |
| Figure 2.6. Influence of three different feeding rates on both particle size and size distributions | 17 |
| Figure 2.7. SEM images of PS-40 core microspheres washed and resuspended in (a)&(b) ethanol and (c)&(d) water | 19 |
| Figure 2.8. SEM images of PS-29 core-shell particles with 2 g PS core and 1 g MTMS [2:1] ... | 19 |
| Figure 2.9. FTIR of (a) PS-31 core/core-shell and (b) PS-36 core/core-shell particles | 21 |
| Figure 2.10. TGA ran in air at 10°C/min. of (a) polystyrene core and (b) polystyrene core-shell samples with varying PS powder to MTMS solution weight ratios | 22 |
| Figure 2.11. FTIR spectrum comparing PS-3 core and PS-3 core-shell particles [2:1] after calcination at roughly 480°C, 500°C, and 520°C | 24 |
| Figure 2.12. FTIR of PS-36 [1:1] after calcination at 1000°C in air | 25 |
| Figure 2.13. PDMS lattice structure (a) CAD and (b) 3D printed specimen..... | 26 |
| Figure 2.14. SEM images of 3D printed PDMS/PFs lattice specimen showing a cluster of hollow spheres within the bulk material | 27 |
| Figure 3.1. Annealing profile of printed PEEK dogbones..... | 32 |

| | |
|---|----|
| Figure 3.2. Ultimate tensile strength of printed PEEK dogbones under five different post-processing conditions..... | 34 |
| Figure 3.3. Young’s modulus of printed PEEK dogbones under five different post-processing conditions..... | 34 |
| Figure 3.4. Stress-strain curve of PEEK specimen sets under five different post-processing conditions..... | 35 |
| Figure 3.5. DMA of printed PEEK from 30°C to 320°C..... | 36 |
| Figure 3.6. DSC curves denoting the percent crystallinity of printed PEEK with different thermal post-processing of (a) unannealed, (b) annealed at 150°C, and (c) annealed at 175°C correlating to samples from the stress-strain curve..... | 37 |
| Figure 3.7. Experimental setup for sulfonating PEEK material | 39 |
| Figure 3.8. TGA curves of PEEK and SPEEK with a heating rate of 10°C min ⁻¹ | 40 |
| Figure 4.1. Solvent casting method of forming CNTs/BTO/PVDF nanocomposites..... | 45 |
| Figure 4.2. Experimental setup and sample preparation for testing multifunctional sensing capabilities | 46 |
| Figure 4.3. Temperature sensing as a function of measured capacitance for various inclusions of CNTs and BTO | 49 |
| Figure 4.4. Stress-strain curve of CNTs/BTO/PVDF nanocomposites and their correlating (b) ultimate stress and (c) ultimate strain | 50 |

Chapter 1: Introduction

The following research work performed embodies three unique studies of polymer structures and their composites. In general, polymers are viscoelastic, insulative materials that are used for a wide variety of applications within industrial, aerospace, and biomedical fields. Polymers have been studied and optimized for any particular use by chemically synthesizing unique micro-structures, altering the physical properties through fabrication and post-processing, and utilizing 3D printing to achieve complex geometries. In the past decade, additive manufacturing (AM) has drawn extensive attention across academia, industry, and government agencies. It offers unprecedented advantages such as design freedom, rapid prototyping, and customization. In this work, three different optimizations of polymer structures coupled with AM were studied to investigate their thermal, mechanical, and electrical properties to produce complex and functional polymeric materials.

First, the development of polysiloxane pore formers were desired to be incorporated into a PDMS matrix for increasing mechanical performance. The formation of monodisperse hollow microspheres is a competitive practice for mass-production manufacturing. Developing uniform pore formers within the range of 5-100 μm was executed by dispersion polymerization where they were loaded into polymer PDMS matrix for 3D printing using a direct write process. By synthesizing the polymer microspheres, it is feasible to control the molecular weight, shell thickness, sphere uniformity, and physical properties as well as lending itself for up-scale production systems. Thus, optimizing the structural integrity and mechanical properties of the 3D printed polymer structures with pore formers can be achieved.

Second, performing thermal post-processing of 3D printed polyetheretherketone (PEEK) to enhance the mechanical properties were studied. Different annealing temperatures and cooling rates employed onto the 3D printed PEEK dogbone specimens provided unique mechanical properties. Achieving theoretical mechanical performance of conventionally molded PEEK through additive manufacturing would further the use of this high temperature polymer.

Combining the freedom of design 3D printing technique with influencing thermal post-processing and printing parameters are shown to critical in the resulting mechanical properties. Also, functionalizing the polymer backbone to increase the electrical performance of the PEEK was done by a process of sulfonation. This functionalization was of interest to identify a fabrication process that utilizes piezoelectric fillers to increase conductivity of the polymer matrix with the intent of fabricating a high-temperature piezoelectric filament.

Third, incorporating a piezoelectric ceramic into a polyvinylidene fluoride (PVDF) matrix that is introduced to an additive manufacturing process was executed. Piezoelectric materials are known to be useful active materials in which they serve as sensors and actuators. Their multifunctional properties derive from their unique capability of coupling mechanical and electrical energy. Thus, the 3D printed multifunctional nanocomposite sensors demonstrated the successful freedom of design methodology paired with improvements in mechanical and electrical properties. Overall, the subsequent three chapters embody different projects, however, they all introduce either synthesized, functionalized, or composite materials into an additive manufacturing process.

Chapter 2: Dispersion Polymerization of Hollow Polysiloxane Microspheres Using Templated Polystyrene Core

2.1 Introduction and Background

Over the past 20 years, there has been an increased interest in nano and micro core-shell particles due to their attractive properties. Although nanoparticles have a larger surface area, microparticle materials are useful for their functional capabilities of storage, absorption, and mechanical properties. Recently, interest in the formation of hollow colloidal particles has risen due to their wide variety of applications such as: energy technologies, impact modifiers, surface coatings, and drug delivery in biomedical applications [1]. Figure 2.1 shows examples of such applications where these hollow microspheres serve as (1) capsules in drug delivery systems where they can be loaded with a cancer-killing drug and eventually rupture using ultrasound once reaching a solid tumor, (2) additives within coatings and cosmetics where the spheres enhance efficiency of UV shielding, (3) enhancing the performance of solar cells caused by the multiple light reflection and strong light scattering, and (4) structural materials to act as shock absorbers when added as pore formers within a surrounding matrix [2-5]. The material of these microspheres as well as the particle size, shell thickness, and surface chemistry are crucial for this projects' desired application of increasing mechanical properties. Two polymeric materials chosen to study their impact on as pore formers to increase mechanical properties of 3D printed elastomeric structures were polystyrene and polysiloxane. Polystyrene (PS) is a hydrocarbon polymer made from the monomer styrene. The synthesized PS particles serve as the templated core which is critical in forming the final particle size of the crosslinked polysiloxane shell. Polysiloxane has a Si-O backbone structure which provides low surface tension, chemical inertness, and is thermally stable. Furthermore, the improvement of existing technology to obtain these functional microspheres with better performance is currently of high interest.

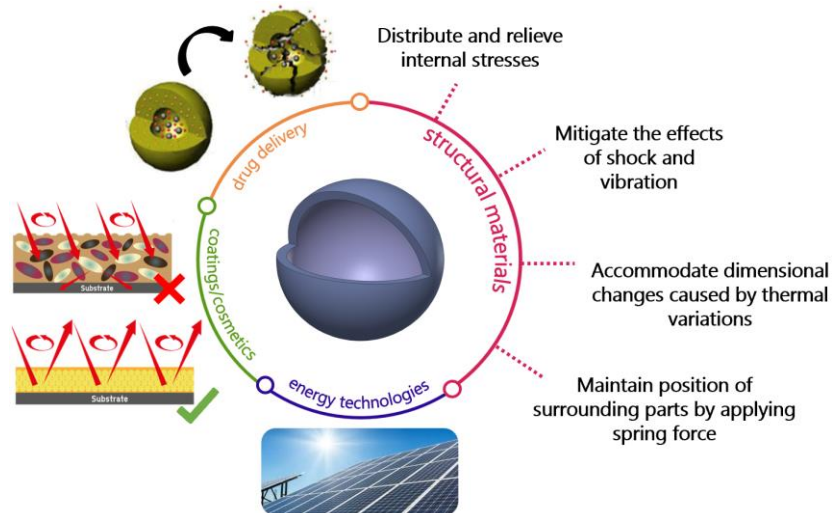


Figure 2.1. Applications of hollow microsphere materials.

2.1.1 Scope of Project

This project is a collaborative research project with Kansas City National Security Campus (KCNSC). The intent was to develop a polymeric foam material from the initial point of chemically synthesizing hollow microspheres used to be dispersed within an elastomeric matrix for producing an additively manufactured product. As mentioned, polymeric foam materials are capable of serving a number of functions for structural materials such as: 1) the distribution and relieving of stresses, 2) mitigating the effects of shock and vibration, 3) accommodating dimensional changes caused by thermal variations, and 4) maintaining the position of surrounding parts by applying the appropriate spring force. With the shift to additive manufacturing processes where 3D structures are built layer by layer being 200 μm or less, there is a need for pore formers with average sizes in the range of 5-100 μm . This project involved developing a process for producing hollow polysiloxane spheres, such as polydimethylsiloxanes, that average in the desired size range that could ultimately be scaled up to a production process. Dispersion polymerization process was determined to be a possible approach to be investigated.

Characterization of the generated microspheres would include size and size distribution, sphere wall thickness, and thermal and mechanical properties.

2.1.2 Dispersion Polymerization

Dispersion polymerization was an attractive reaction because of its easy execution process, high yield of particles, and ability to be a large-scale process for several applications. The polymerization also lends itself to produce particles with a narrow size distribution [6,7]. In this case, the method is a heterogenous polymerization process where a vinyl monomer is paired with an initiator that are introduced into a medium of organic solvent(s) and steric stabilizer. Although the initiator and monomer are soluble in the medium, the polymer is not, making the polymerization heterogenous [8]. Distinctly, this process can be understood as a two-stage process: 1) the nucleation stage and 2) the growth stage. The first stage, which is greatly affected by the solvency of the medium, is more delicate and complex because it includes when the oligomers present in the reaction form the precipitating nuclei. Alternatively, the growth stage takes up the bulk of the reaction time in which the rest of the monomers from the surrounding solution (continuous phase) are absorbed by the nuclei to facilitate particle growth [9]. Also, the presence of the stabilizer is to be adsorbed onto the developed polymer particles to promote stability which reduces undesired coagulation. As a result, the diameters of the synthesized polymeric spheres obtained are typically 0.5-10 μm .

2.2 Chemical Synthesis

The growth of core PS particles was increased from 0.5 μm to 8 μm due to varying the initial state of polymerization (chemical reagents, temperature, concentrations), experimental setup, and rate kinetics. It should be noted that only highlighted synthesis trials will be examined for validating the progression of the final experimental procedure.

2.2.1 Experimental Materials

Reagents used for different synthesis trials included: styrene (St, 99% extra pure, ACROS Organics), 3-(trimethoxysilyl)propyl methacrylate (TMSPMA, 98%, Sigma-Aldrich), polymethylmethacrylate (PMMA, $M_w=15,000$, Sigma-Aldrich), divinylbenzene (DVB, Technical Grade 55%, Sigma-Aldrich), 2-methoxyethanol (MeCell, 99+% extra pure, Acros Organics), ethanol (EtOH, 200 proof, Pharmco), polyvinylpyrrolidone (PVP, $M_w=40,000$, Sigma-Aldrich), hydroxypropyl cellulose (HPC, $M_w=100,000$ g/mol, Acros Organics), Azobisisobutyronitrile (AIBN, 12 wt% in acetone, Sigma-Aldrich), benzoyl peroxide (BPO, EMD Millipore Corp), trimethoxymethylsilane (MTMS, Sigma-Aldrich), hydrochloric acid (HCl, Fisher Scientific), and ammonium hydroxide solution (NH_4OH , Sigma-Aldrich). Vacuum distillation studies were done to the commercial styrene to remove the 4-tert-butylcatechol inhibitor, however, the observed performance showed negligible improvement towards increasing particle size. Therefore, supplied reagents were used with no further post-processing/purification. PDMS 1700 (KCNSC provided) and 184 silicone elastomer (PDMS 184, Sylgard) were used as the polymer matrix for 3D printed structures.

2.2.2 Formation of Core

Final core microspheres were synthesized by dispersion polymerization where MeCell (250 mL), EtOH (175 mL), and HPC (7.5 g) were weighted into a 1000-mL five-neck glass reactor equipped with a teflon stirrer, reflux condenser, and nitrogen inflow as shown in Figure 2.2. To ensure a homogeneous mixture, the reactor was submerged into ethylene glycol to act as a heated blanket. First, the system was purged with nitrogen for 30 min. to remove any oxygen within the vessel while the solution was stirred at 480 rpm to dissolve the HPC. Then, the flask was heated to 75°C. Styrene (75 mL) and BPO (3 g) were then added at a feeding rate of 5.2

mL/min using a serological pipette. After dispensing the monomer and initiator, the solution visibly transitioned from clear to white after 10 min. The reaction was carried out for 24 hrs. Polystyrene (PS) cores were collected by centrifuging, decanting, and resuspending for two washes using denatured ethanol to remove any residual reagents and surface-anchored stabilizer. The precipitated pellet was left in a desiccator to dry overnight.

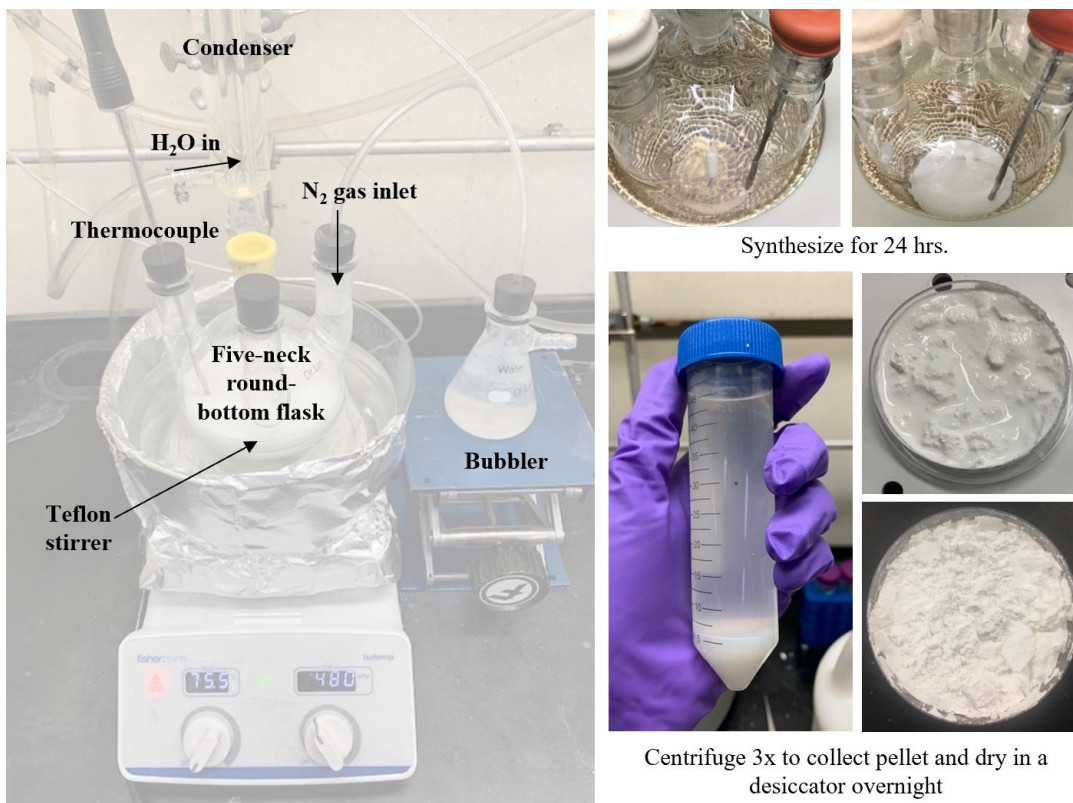


Figure 2.2. *Experimental setup for dispersion polymerization of polystyrene.*

2.2.3 Mechanism for Free-Radical Initiation of Polystyrene

The addition polymerization (kinetic chain reaction) of the styrene monomer consists of three steps: initiation, propagation, and termination [7,8]. Within the initiation stage, free radicals derived from the initiator are catalytically generated by heat. These radicals open the double bonded monomer, making a reactive center where a styrene monomer with unpaired electrons attacks another double bond. As a result, the chain grows by successive addition of monomer

units with unpaired electrons shifting toward chain ends with each new mer known as the propagation step. This formation of long polymer chains eventually ceases typically because one unbound electron meets another unbound electron, thus, terminating polymer growth also considered as the meeting of two free radicals [8].

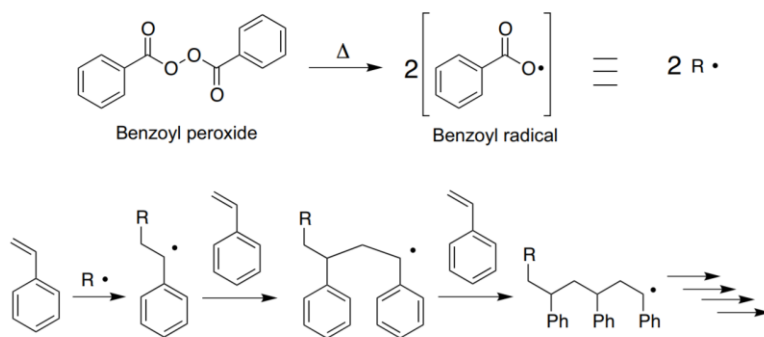


Figure 2.3. Depiction of radical initiation of BPO for the addition polymerization of styrene [10].

2.2.4 Factors Contributing to Particle Size of Templated Core

The control of particle size and uniformity prepared by the dispersion polymerization system has been a challenge within the polymer science community when attempting to obtain microspheres greater than 3 μm . Overcoming this limitation of dispersion, namely the nature of dispersion polymerization, is typically achieved by using different types and concentrations of the reagents, increasing temperature, and manipulating polymerization kinetics.

2.2.5 Hydrolysis and Condensation of MTMS

Single-shell hollow polysiloxane spheres were formed by a sol-gel process; polystyrene core particles are shelled from a two-step catalytic procedure involving MTMS. Polystyrene cores (2 g) ground into a fine powder, DI water (5 g), and MTMS (1 g) were added into a 5-pH solution using HCl as the catalyst [11]. The hydrolyzed system was sonicated for 10 min. to provide a homogenous dispersion of the resulting silanols from the hydration reaction. Then, ammonium hydroxide was added into the same solution to achieve a pH between 8.5-9.5

facilitating the condensation reaction of the MTMS for 5 hrs. This resulted in formation of siloxane (Si-O-Si) units by the elimination of water where these polymer chains were localized on the core particle surfaces [11]. Although polystyrene does not have a high affinity towards these siloxane networks, it has been found that the adsorbed stabilizer is what promotes the hydrogen bonding of the shell [8,11]. Furthermore, the hydrolysis and condensation are represented by the following chemical reactions [12,13]:

1. Hydrolysis (hydration reaction):



2. Condensation (dehydration reaction):



The resulting pellet was recovered after decanting and left to dry overnight in a desiccator. Subsequent core-shell (polystyrene-polysiloxane) particles were then calcinated at 500°C in air for 3 hrs to evaporate the core and recover hollow microspheres [11].

2.3 Results

2.3.1 Growth of Templated Particles

Another study was proposed where the authors developed a simple method of preparing micron-sized hollow polysiloxane spheres by first synthesizing polystyrene cores in the 1-4 μm range using small quantities of AIBN (0.1 g), PVP (2.5 g), water/EtOH medium (4 g/36 g), styrene (10 g), and TMSPMA (1 g) [11]. However, although the experiment introduced TMSPMA copolymer to facilitate particle growth and increase affinity with the MTMS shell, their reactants failed to produce particles in the desired range of 5-100 μm, therefore, different relationships of the medium solvency were needed. The importance of manipulating the solvency of the medium has been addressed as a critical factor in impacting the size and

dispersity of the polymer microspheres [14,15]. The addition of MeCell rather than having a medium of water and EtOH was found to reduce the polarity of the medium which further increased particle size as well as polydispersity. The differences of solubility parameters between water ($\delta = 23.4$), EtOH ($\delta = 12.7$), and MeCell ($\delta = 11.4$) as a function of monomer concentration varied the reaction negatively by limiting the ability to produce uniform polymer particles. However, it was discovered that only coupling EtOH and MeCell provided the preparation of 5-10 μm particles when having a 30 vol% EtOH/55 vol% MeCell (15 vol% styrene) reaction concentration [15,16].

Although increasing particle size was a direct requirement for this project, controlling the uniformity of the particles was important to have repeatable mechanical testing when these added pore formers were introduced into the PDMS matrix for printing. A dropwise feeding method has been demonstrated before where both monomer and initiator were fed into the reaction medium at the elevated temperature [17]. It was discovered that at appropriate feeding rates, a narrow particle size distribution could be obtained for spheres in the region of 5-7 μm . These uniform particles are related to the available free monomer concentration in the continuous phase, decrease of coalescence reactions from the enhanced stabilizer adsorption, and proper elongation of the nucleation period [15,16]. For example, if the feeding rate is too slow, large particles appear due to a prolonged nucleation period and excessive solvency of the continuous phase. If a feeding rate is not used, there is a risk of having little particles form due to the higher consumption of monomer leading to less stability of the formed particles and an increase in coalescence. As a result, exploring the addition of monomer at a rate based on the rate kinetics of the styrene and initiator could provide more uniform microspheres depending on the types of ingredients and reaction concentrations.

Another consideration for the polymerization of the polystyrene microspheres was if the purification of styrene using vacuum distillation or commercially packed columns with alumina had any effect on the particle growth. Commercial styrene typically contains a stabilizer (4-tert-butylcatechol, TBC) used to prevent polymer formation and oxidative degradation for storage purposes. Inhibitors could prevent polymerization either by typically disarming the growing chain with free-radicals or by acting as antioxidants [18,19]. However, using both methods of styrene purification produced no distinct differences verified by GC-MS and NMR. Therefore, there was no evidence to suggest that the styrene was distilled improperly; the inhibitor did not cause the particle size of the produced polymers to be significantly constrained.

As a result of the experimental variations mentioned regarding the ratio of monomer and comonomer, manipulating the medium, and rate addition of monomer/initiator where AIBN and PVP were used as the initiator and stabilizer, respectively, these investigations were not enough to produce particles past the minimum threshold of 5 μm in their average diameter size. Therefore, these upcoming efforts executed in this body of work provided the most promising polystyrene microspheres regarding particle growth and low coefficient of variation (CV). In order to obtain monodisperse 10 μm particles, the following concentrations were used: 175 mL EtOH, 250 mL MeCell, 75 mL Styrene, 7.5 g HPC, and 3.0 g BPO reacted at a temperature of 65°C for 2 hours then increased to 75°C for 24 hours [16]. The reactions employed for this study included these exact quantities with different temperatures and feeding rates of monomer/initiator. Additionally, HPC and BPO were supplemented instead of AIBN and PVP, respectively, for several reasons: 1) HPC is a nonionic cellulose ether that is soluble in both water and a number of organic liquids and is suitable in decreasing steric stabilization when polymerization rate increases, therefore, increasing particle size [20], 2) BPO is processed using water which is then

dehydrated into a powder; the remaining residual water can help form a dissolution bridge between MeCell and EtOH solvent medium to increase the level of monodispersity and decrease the CV [14], and 3) the decomposition and free-radical formation of BPO has a wider temperature range of 60-140°C [21]. The following trials summarized in Table 2.1 were performed showing the effect temperature, monomer feeding rate, and comonomers had on particle growth and size distribution.

Table 2.1. *Effect of temperature and feeding rate and PS core microspheres.*

| Sample | Temperature (°C) | Feeding Rate (mL/min) | Particle Size | |
|--------------------|----------------------|-----------------------|-----------------------|------------|
| | | | D _{avg} (μm) | CV (%) |
| PS-29 | 65(2hrs) - 75(24hrs) | - | 3.55 | 1.72 |
| PS-31 | 65(2hrs) - 75(24hrs) | 5.2 | 4.58 | 3.18 |
| PS-33 | 65(2hrs) - 75(24hrs) | 4 | 3.70 | 3.16 |
| PS-36* | 65(2hrs) - 75(24hrs) | 5.2 | 2.49 | 3.88 |
| PS-38 | 70(2hrs) - 75(24hrs) | 5.2 | 4.66 | 2.67 |
| PS-39 ^p | 75(24hrs) | 5.2 | 6.30, 6.43 | 9.30, 7.79 |
| PS-40* | 75(24hrs) | 5.2 | 8.20 | 9.65 |

*included comonomer

^pPS-39 run twice for proof of accuracy

All chemical compositions are the same, however, PS-36 had a 9:1 weight ratio of St to PMMA comonomer while PS-40 included a 10:1 weight ratio of St to DVB cross-linker, respectively [22,23]. Hence, PMMA was introduced with styrene at the start of polymerization while the 1wt%DVB was added an hour after styrene was fed into the reaction and reached a stable 75°C. The average particle diameters were determined by averaging values between MATLAB and Image J where roughly 100 particles were considered for each method. For MATLAB, the `imfindcircles` function was used and modified for every image by changing the pixel range, sensitivity, edge threshold, and scale to determine the generated particle diameters in microns. Alternatively, Image J was used by manually setting the scale with relation to the pixels

then collecting data by measuring particles using a straight line. As for particle distribution, the coefficient of variation was defined using Eq. 2.1:

$$CV\% = \left(\frac{SD}{\bar{X}} \right) \times 100 \quad (2.1)$$

where CV denotes the coefficient of variation, SD denotes the standard deviation, and \bar{X} denotes the average particle diameter.

SEM images shown in Figure 2.4 depict the PS cores obtained using dispersion polymerization. Subsequently, as the initial temperature of the reaction increased, the average particle diameter for these micron-sized PS cores increased from 5-8 μm . The polystyrene microspheres had a narrow size distribution, where the CV's were <10%, constituting these trials to be monodisperse. Additionally, PS-29 produced the smallest particles ($D_{\text{avg}} = 3.55 \mu\text{m}$), however, produced the most uniform microspheres which highlighted the inverse relationship between size and uniformity; it is critical in determining the equilibrium point of decreasing polydispersity when altering temperature, rate, and/or additives to increase particle size. The trials solely effected by increasing temperature produced a linear increase in average diameter due to an increased rate of polymerization where PS-31 ($D_{\text{avg}} = 5.44 \mu\text{m}$), PS-38 ($D_{\text{avg}} = 5.58 \mu\text{m}$), and PS-39 ($D_{\text{avg}} = 6.37 \mu\text{m}$).

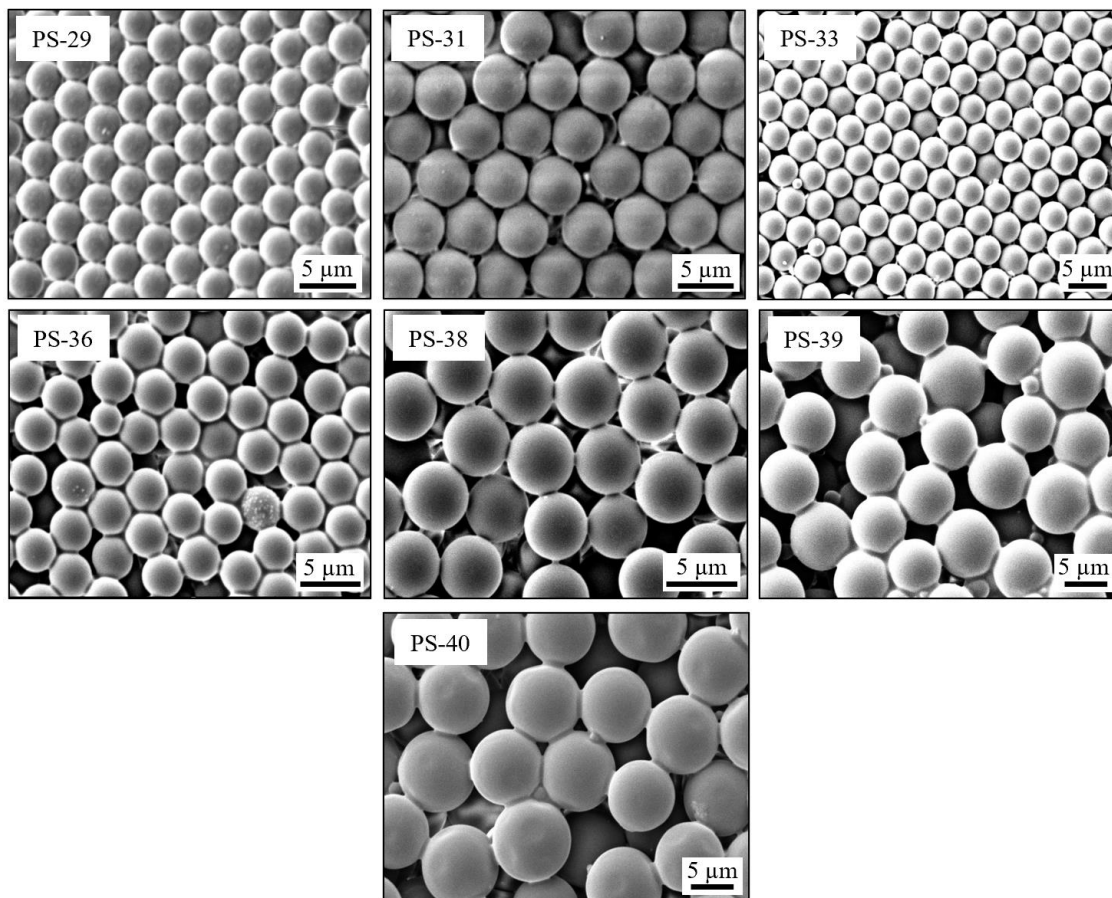


Figure 2.4. SEM images of polystyrene core microspheres with the corresponding reactants from Table 2.1.

Temperature significantly influences kinetics of initiator decomposition and medium solvency for oligomeric radicals where the critical chain length of the forming oligomer chains increases which decreases the molecular weight of the final particles [8,15,16]. As a result, there is a significant decrease of precipitated oligomeric radicals within the continuous phase, which produces fewer nuclei thus leading to larger particle size [15]. Also, the adsorption rate of grafted HPC-stabilizer is less effective since they are more soluble which increased the extent of primary particle coagulation [20]. These variations in temperature are only employed within the first two hours because the monomer conversion has been shown to stabilize where the particles converge from the nucleation phase into the growth phase [15,24]. This thermal influence on the polymerization of PS microspheres is summarized in Figure 2.5.

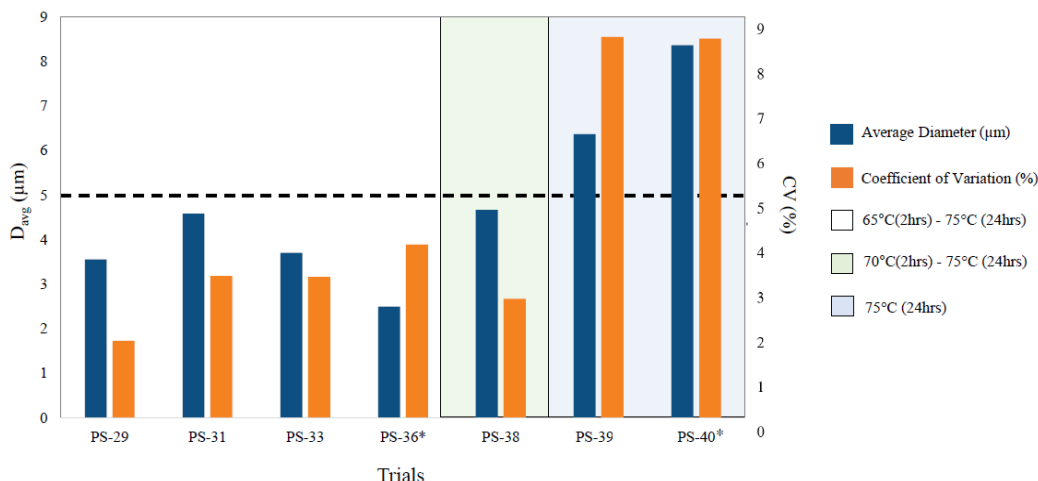


Figure 2.5. Effect of temperature on the average diameter and coefficient of variation of the templated polystyrene microspheres.

Next, determining the impact on particle size and distribution as a function of feeding the monomer/initiator at a rate into the continuous phase was studied. As shown in Figure 2.5, the first three trials within the same temperature profile (PS-29, PS-31, PS-33) exhibited an increase in particle size and size distribution when feeding the monomer/initiator solution at a fast rate of 5.2 mL/min. found in a previous study [17]. This particle increase can be analyzed from general rate kinetics of the controlled dispensing of styrene and BPO initiator within the free-radical chain polymerization process where particle nucleation and growth steps are impacted. To determine these kinetic values, published data by researchers utilizing similar systems and reactants consider a first-order condition of monomer based on the half-life decomposition rate of the initiator for simplification [8]. Rate kinetics is also highly temperature-dependent; however, the 5.2 mL/min. rate was kept for higher temperature reactions for consistency and comparisons. Recalculated feeding rates are to be introduced in the next phase in experimentation. According to Eq. 2.2, the bulk reaction rate is derived from the rate kinetics of polymerization principle:

$$r = k_1[R] + k_2[R][P] \quad (2.2)$$

where r denotes the reaction rate, R denotes reactant concentrations, P denotes autocatalytic product concentrations, k_1 denotes non-catalytic rate constant, and k_2 denotes catalytic rate

constants. Products are considered autocatalytic meaning once the BPO free radical reacts with styrene monomer, the chain propagation is initiated and continues solely without further initiation until the chain terminates. Assuming polystyrene follows an autocatalytic reaction and the concentration of the BPO free radical is small and constant, $d[R]/dt = 0$ thus, steady state can be applied. Although Eq. 2.2 gives an overview of the rate polymerization as a function of the constituent reactants and products, the following equation specifies more clearly the effect of half-life assumption for initiator within this first-order derivation:

$$R_p = k_p[M][I]^{1/2} \left(\frac{k_d f}{k_t} \right)^{1/2} \quad (2.3)$$

where R_p denotes rate of polymerization, M denotes the monomer concentration, I denotes initiator concentration, k_d denotes rate constant of the initiator decomposition, k_t denotes rate constant for termination, k_p denotes rate constant of monomer propagation, and f denotes the efficiency factor of the initiator [8,25]. Combining the rate constants in Eq. 2.3 results in the simplified first order reaction:

$$R_p = k_p[M][I]^{1/2} \quad (2.4)$$

where R_p denotes rate of polymerization, k_p denotes rate constant of monomer propagation, M denotes the monomer concentration, and I denotes initiator concentration. Reducing Eq. 2.2 to Eq. 2.4 increased the ease of calculation. The rate constants in these equations were calculated using published kinetic and thermodynamic data on styrene and BPO systems. For future work, collecting aliquots to determine the % monomer conversion and configuring simulations of the polymerization system will facilitate greater accuracy of the propagation and termination rates in our polymerization system [25]. The proper monomer feeding rate is critical to produce large, uniform particles in a dispersion polymerization system.

During dispersion polymerization, the growth of microspheres occurs because of the interaction between free radicals and available monomer which results in coalescence between

particles. Introducing a feeding rate into the dispersion polymerization system causes the free monomer concentration to increase due to a slower conversion of monomer to polymer [15]. Additionally, the free monomer concentration is directly proportional to the solvency of the medium [19]. An increase in solvency paired with an increase in free radical concentration results in better stability, longer nucleation periods, and a decrease in the number of growing particles. The smaller the number of growing particles the larger amount of stabilizer adsorbed on the particles resulting in the better stability and reduction in coalescence.

Two important factors that dictate particle uniformity include having a long nucleation period and preventing the coalescence of particles in the growth phase [11,14]. Monodispersity is dependent on the monomer dosage rate [15]. To obtain monodisperse particles the feeding rate must fall in a small window of equilibrium where there are fewer nucleation reactions, a longer nucleation period, and little to no coalescence reactions. If the rate is too slow, the monomer concentration inside the particles decreases which leads to a reduction in propagation rate resulting in an overall reduction in volumetric particle size [15,17]. If the rate is too fast, the monomer concentration and consequently the particles will be polydisperse. Such investigations were employed and are seen in Figure 2.6.

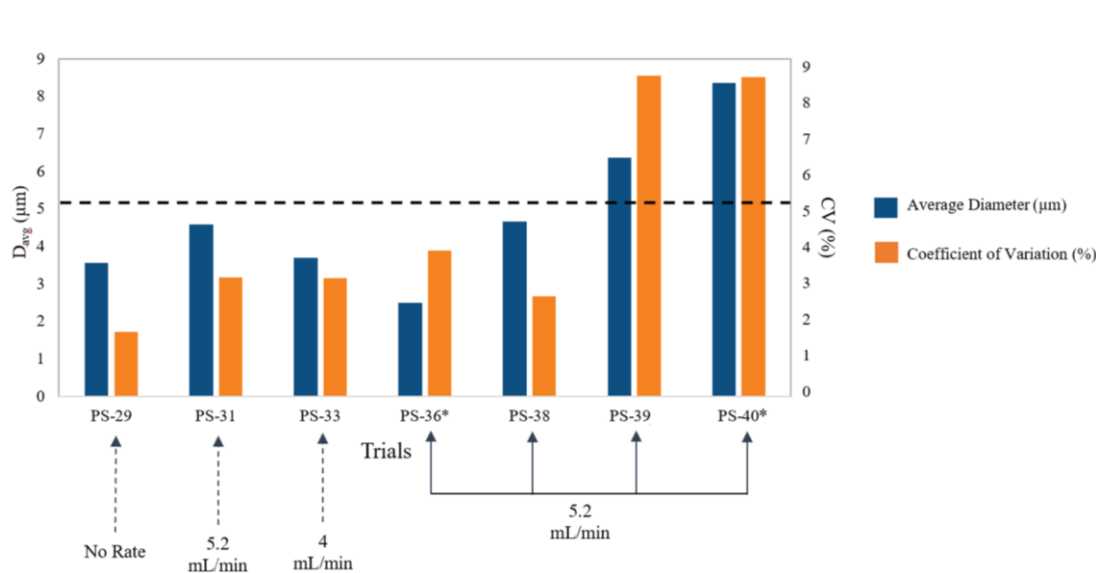


Figure 2.6. Influence of three different feeding rates on both particle size and size distribution.

Primary focus on comparing the first four trials run at the same temperature as the control as shown. Between PS-29 through PS-33, the fastest rate of 5.2 mL/min. increased particle size and the coefficient of variation. Since at the time the focus was to pass the 5 μm threshold and feeding rate showed promising increase in particle size, we decided to keep the 5.2 mL/min. for the subsequent trials. For PS-36 we found that when introducing more PMMA than styrene, it resulted in inhibiting the growth of styrene. Therefore, altering the rate and monomer concentrations would fix this issue, however, increasing temperature was any easier route to try first. Ultimately, temperature had the greatest effect on increasing size and the feeding rate is needed for promoting dispersity rather than particle growth for our system. Seeing how PS-40 yielded the largest most uniform particles, further focused investigations are needed to establish the reproducibility and the effects of temperature and comonomer.

An interesting phenomenon happened when collecting the PS-40 particles where washing and resuspending them in ethanol vs. water gave different visual distributions as seen in Figure 2.7 theoretically due to polarity. For this study, DVB was added an hour after the polymerization process of styrene begun at a rate of 4 $\mu\text{L}/\text{min}$. The addition of DVB after one hour is done because DVB monomer is more reactive than styrene. Therefore, including this crosslinker when polymerization rate of styrene starts to level off is needed to avoid secondary nucleation [23,26]. The particles seemed to be more uniformly distributed in ethanol where the average diameter was 8.20 μm (9.66% CV). In water, the microspheres had an average diameter of 5.53 μm (50.7% CV) constituting them as polydisperse or even bimodal. Although the average of the particles in both suspensions were greater than 5 μm , the CV's are extremely different deeming one as monodisperse and the other polydisperse. Moving forward, key changes in the synthesis and post-processing would optimize these results including: (1) reducing the rate or extending

the time DVB was added into the medium to avoid secondary nucleation or (2) not implementing a rate for the styrene monomer entirely for comparisons. Although we successfully grew the core particles, they ultimately serve as a template core for the desired polysiloxane hollow microspheres.

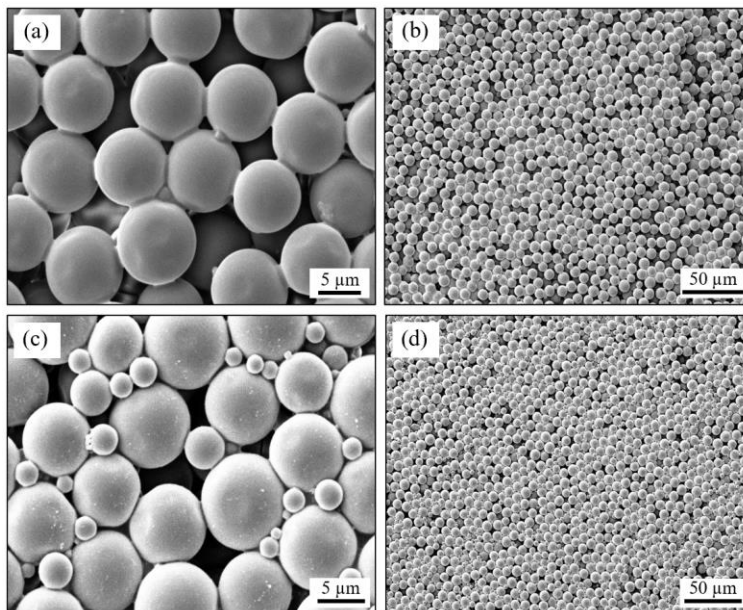


Figure 2.7. SEM images of PS-40 core microspheres washed and resuspended in (a)&(b) ethanol and (c)&(d) water.

2.3.2 Crosslinking of Polysiloxane Shell

The resulting formation of the siloxane network onto the PS microspheres via a sol-gel process was shown to successfully produces smooth outer-surfaces as shown in Figure 2.8. Properties of the polysiloxane are needed using analytical chemistry to better understand the type and number of side groups, molecular weight, and crosslinking density.

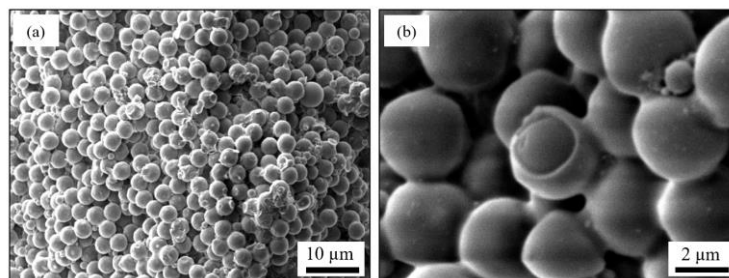


Figure 2.8. SEM images of PS-29 core-shell particles with 2 g PS core and 1 g MTMS [2:1].

Although the morphology of the spheres clearly shows the core-shell formation present in Figure 2.8(b), investigations were conducted to study different monomer content ratios between core and shell to the process. Studies have been shown where weight ratios less than 1:1 were used to form latex systems, insufficient amount of polysiloxane would not provide an even amount of coating onto the core microspheres [22]. Alternatively, ratios greater than 1:3 where the presence of more organosilicon increased the viscosity of the catalytic solution which depleted the cross-linking effect with the core particles [22]. Therefore, studying the effect of different monomer content on lessening or enhancing our core-shelling processes of obtaining fully coated spheres with reduction in siloxane agglomerations was important. PS-31 and PS-36 particles with different weight ratios of core to shell were selected for this study because of their relatively large size (at the time) and inclusion of comonomer. Studies have shown where introducing a comonomer such as TMSPMA or PMMA promote greater cross-linking of the silanes resulting in more smoother shells with higher molecular weight [11,22,27]. The weight ratios investigated were 2:1, 1:1, and 1:2 which reflect the following relationships: more PS cores to MTMS, equal parts PS core to MTMS, and more MTMS to PS core inclusions into the sol-gel process, respectively. It was assumed that the 1:2 relationship would result in more weight loss % difference than the other two which would be attributed to an increased formation of silanols, however, this was not the case reflected in the following thermal investigations.

Fourier-transform infrared analysis (FTIR) was performed between a 600-4000 cm^{-1} wavenumber range at room temperature to validate the presence of Si-O groups using the sol-gel method for PS-31 and PS-36 shown in Figure 2.9. IR absorption bands at 1640 cm^{-1} and 3350 cm^{-1} can be attributed to absorbed water or solvent after vacuum drying. The IR characteristic bands for PS core were easily identified by the following: aromatic C-C out of plane bend at 694 cm^{-1} , aromatic C-H bend at 756 cm^{-1} , aromatic C-C stretch vibration at 1451 cm^{-1} , and aromatic C-H stretch vibration at 1492 cm^{-1} [11,28].

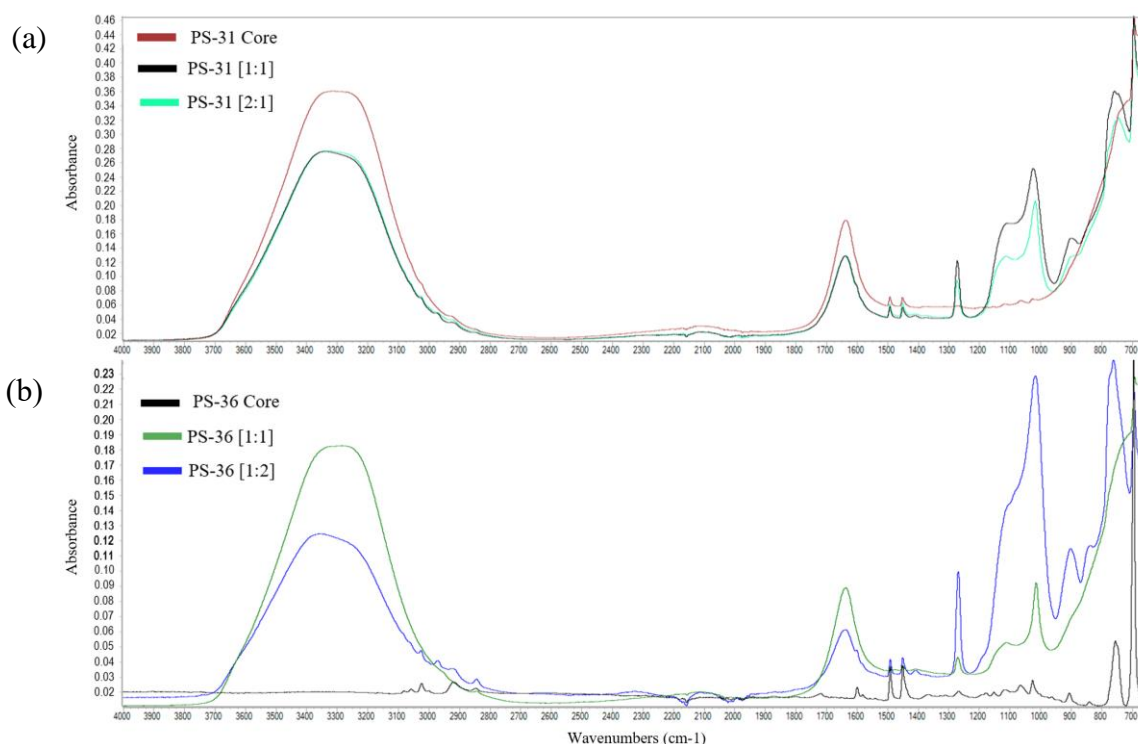


Figure 2.9. FTIR of (a) PS-31 core/core-shell and (b) PS-36 core/core-shell particles.

There is also a peak that more distinctly shows an aromatic C=C stretching at 1600 cm^{-1} for PS-36 core which was attributed to the lack of absorbed solvent. Polysiloxane bands are identified for both PS-31 and PS-36 microspheres with different ratios of core to shell deduced by the following bands: asymmetric Si-O-Si vibration at 1017 cm^{-1} and Si-CH₃ group found at 1272 cm^{-1} [29]. Overall, the polysiloxane shell was successfully identified and differentiated from the polystyrene core proving the polysiloxane material, specifically defined by the -CH₃ group, was

formed throughout the various ratios. However, several bands in the 600-900 cm^{-1} and 2800-3200 cm^{-1} ranges were convoluted and FTIR could not quantitatively determine the extent of shelling onto the PS core. Therefore, further investigations to gather shell thickness and thermal degradation were desired.

2.3.3 Calcination of Hollow Polysiloxane Microspheres

To remove the PS cores forming the inner void, calcination of polystyrene was performed to thermally degrade the polymer at high temperature while retaining the polysiloxane shell. This calcination process was done by introducing the dried core-shell particles into a furnace at 500°C in air for 3 hours with heating and cooling rates of 10°C/min [11]. The samples investigated were PS-2, PS-3, PS-29, PS-31, and PS-36. Earlier trials (PS-2 and PS-3) impacted by this thermal treatment process displayed the presence of polysiloxane and the loss of polystyrene using FTIR shown in Figure 2.11.

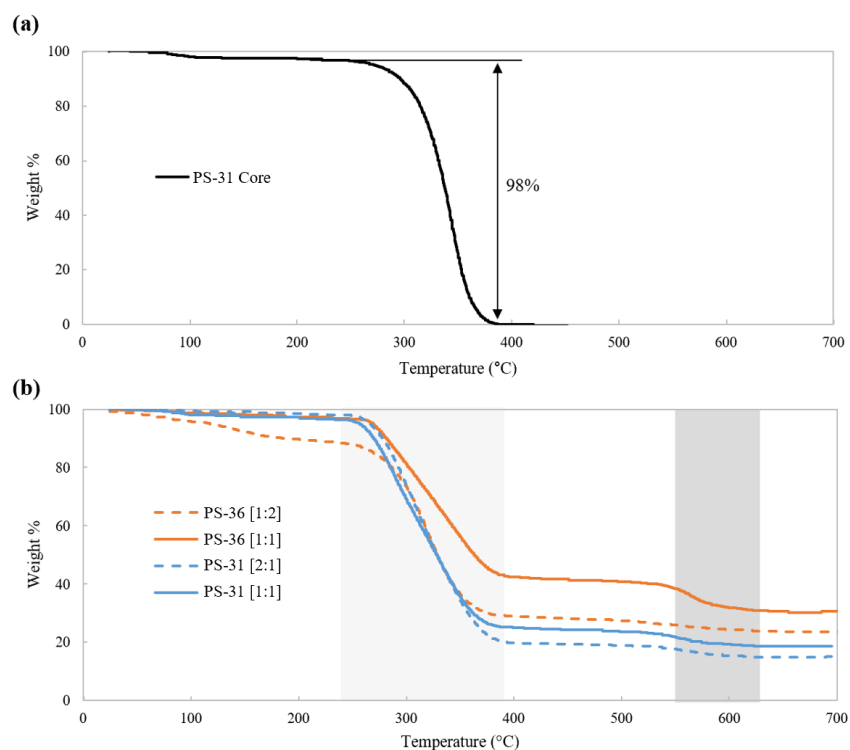


Figure 2.10. TGA ran in air at 10 °C/min of (a) polystyrene core and (b) polystyrene core-shell samples with varying PS powder to MTMS solution weight ratios.

Although the FTIR results showed the different bonds present for polystyrene and polysiloxane, determining the thermal degradation regions and correlation between shell thickness was done using TGA. Thermogravimetric analysis (TGA) was performed up to 700°C in air with a heating rate of 10°C/min. on shelled PS-31 and PS-36. In Figure 2.10(a), the onset and endset of the complete thermal degradation of the polystyrene cores was 315°C and 362°C, respectively, with 98% weight loss. The initial 2% weight loss can be attributed to the burnout of residual water or solvent. However, the core-shell particles in Figure 2.10(b) produced two weight loss regions. Region 1 shows weight loss in a range between 263°C and 376°C where roughly 55-80% of the samples were degraded. This shows where the less thermally stable polystyrene and PMMA core particles are reduced. Region two shows a second weight reduction between 513°C and 593°C where the methyl group from the polysiloxane shell is degraded, leaving roughly 15 wt% of residue remaining for all the samples up to 700°C [11]. The ratios of 1:1 for both PS-31 and PS-36 demonstrated larger weight loss than their counterpart. Therefore, it's assumed that for these three varieties tested (1:2,1:1,2:1), the 1:1 relationship of PS core to MTMS shell introduced into the acid-base catalytic sol-gel process facilitated more stable shelling of polysiloxane. Further studies using small-angle x-ray scattering (SAXS) were to be employed to quantitatively determine shell thickness.

Different calcination temperatures at 480°C, 500°C, and 520°C (heating rate=10°C/min. in air) on PS-3 core-shelled [2:1] particles to study the impact the thermal environment on the polymer structures and determine if optimization of dwell temperature was required. These samples were then compared using FTIR as shown in Figure 2.11.

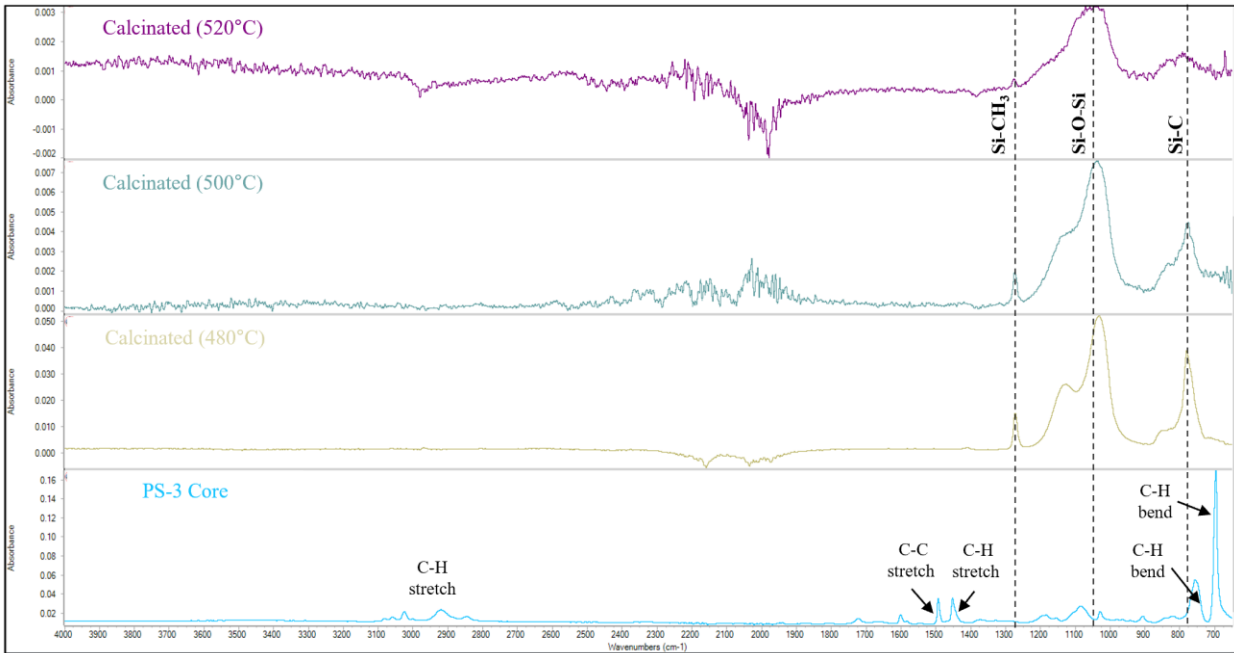


Figure 2.11. FTIR spectrum comparing PS-3 core and PS-3 core-shell particles [2:1] after calcination at roughly 480°C, 500°C, and 520°C.

Similar IR characteristic bands of PS-31 and PS-36 specimens in Figure 2.9 are seen, however, the Si-CH₃ group at 1272 cm⁻¹ seemed to have less intensity at 520°C which could possibly be attributed to the transformation of MTMS (a ceramic precursor) into silica. Additionally, a Si-C stretch at 775 cm⁻¹ can be more easily identified from the PS-3 sample than from the previous PS-31 and PS-36 FTIR study. Although the transition of polysiloxane into silica cannot be completely verifiable by this peak depletion from Figure 2.11(a), PS-36 [1:1] was calcinated at 1000°C for 1 hour to study the polymer-ceramic transition. The residue powder collected after being introduced to this high temperature not only removed the distinctive methyl group at 1272 cm⁻¹, but also maintained the hollow spherical shape as shown in Figure 2.12. As a result, this demonstrated the possible feasibility of forming hollow silica spheres as well, although the exact transitioning temperature is still unknown.

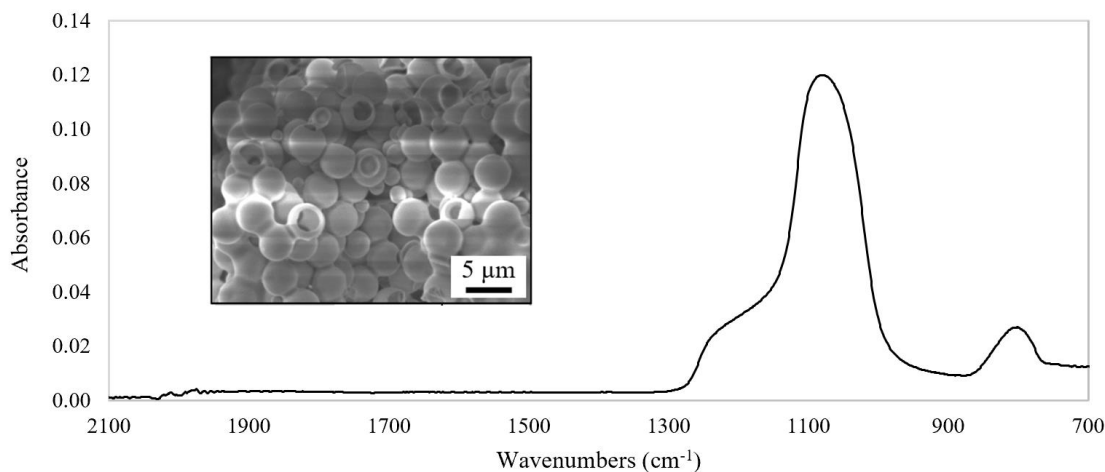


Figure 2.12. FTIR of PS-36 [1:1] after calcination at 1000 °C in air.

Furthermore, analyzing this relationship between degradation of polystyrene while maintaining polysiloxane before transition into silica is required to optimize calcination temperature. Improving this calcination process by changing the heating rate, dwell temperature, and testing in inert environment are the next necessary steps.

2.3.4 Additive Manufacturing of Pore Formers

The preparation of polymeric paste constituted of several steps. First, the two-part silicon elastomer polydimethylsiloxane (PDMS 1700) provided by KCNSC was mixed in a 10:1 weight ratio (base elastomer : curing agent). Separately, PDMS 184 (Sylgard) was mixed in the similar fashion. These two mixtures were left in a vacuum desiccator to degas for 30 min. Then, the two elastomers were hand-mixed using an 8:2 paste formulation of PDMS 1700 and PDMS 184, respectively. This allowed the less-viscous PDMS 184 material to dilute PDMS 1700 for enhanced flowability and mechanical properties [30]. Characterizing this paste was done at room temperature using a DHR-2 rheometer (TA Instruments) with a 1.5 mm gap. A resulting good shear thinning behavior was observed which grants proper flowability and printability of the green body. Lastly, 40 vol% hollow polysiloxane microspheres (PS-29) were incorporated into

the PDMS matrix by grinding the dried powder and hand mixing the microspheres into the elastomeric matrix until it became visibly homogenous. This relatively lower level of microsphere inclusions (pore formers) was selected to first test printing feasibility and analyze particle distribution. PS-29 hollow spheres were selected due to its monodispersity and relatively large size for generating preliminary data; further inclusions are to be done. Also, the hollow spheres were assumed to be equal in size ($3.55 \mu\text{m}$) as well as shell thickness ranging between 100-180 nm for calculating %inclusion.

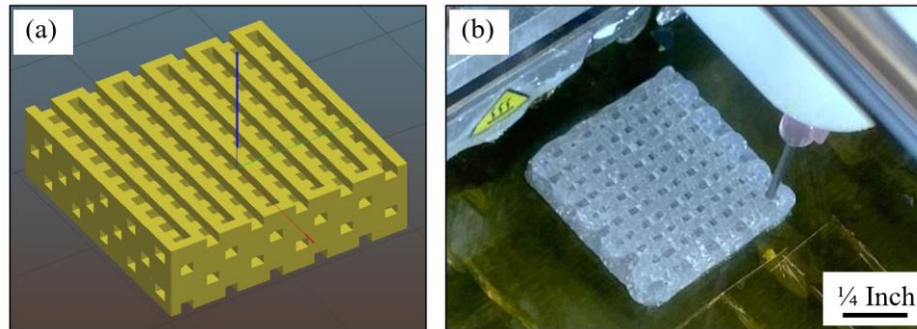


Figure 2.13. PDMS lattice structure (a) CAD and (b) 3D printed specimen.

These samples were printed onto a thin metal plate with a layer of Kapton tape using a modified FDM 3D printer (Ultimaker 2+) to allow for printing porous elastomeric structures for expected testing of enhanced mechanical properties. Figure 2.13(a) shows the CAD of the lattice geometry ($19.09 \times 19.09 \times 5.6 \text{ mm}$) in Slic3r which was used to demonstrate the level of accuracy of a complex geometry. The lattice encompassed 90° raster of continuous infill where each individual strut had three layers of continuous material. A 3D printed fixture fastened the 50cc syringe where a piston applied force to the loaded syringe to extrude the paste which fed into teflon tubing connected to the extruder head seen in Figure 2.13(b). The nozzle used for printing had an outer diameter of 0.91 mm and inner diameter of 0.6 mm. The build plate was

calibrated to the nozzle prior to printing, while the speed was set to the maximum value until the paste began extruding then decreased to a level of continuous material flow.

After the sample was printed, the aluminum plate was removed from the bed and placed into a UV curing chamber (Formlabs) at 70°C for 30 min. The cured specimen was cut and sputter coated with a copper target for 5 nm layer thickness to investigate the cross-section of the lattice strut using SEM images as seen in Figure 2.14. The closed-cell pore formers (PFs) revealed to be non-uniformly dispersed within the PDMS matrix as a result of poor mechanical mixing where agglomerations of packed porosity are denoted in Figure 2.14(a). This will later be optimized with the use of a Thinky Mixer to mix, disperse, and deaerate the paste for future prints. The included particles did, however, maintain their shape and seemed to have only roughly 20% decrease in shrinkage where $D_{avg}=3 \mu\text{m}$ after calcination. Also, optimizing the shelling process to alleviate coagulation of particles resulting in singular, ultra-thin shells on the individual PS cores.

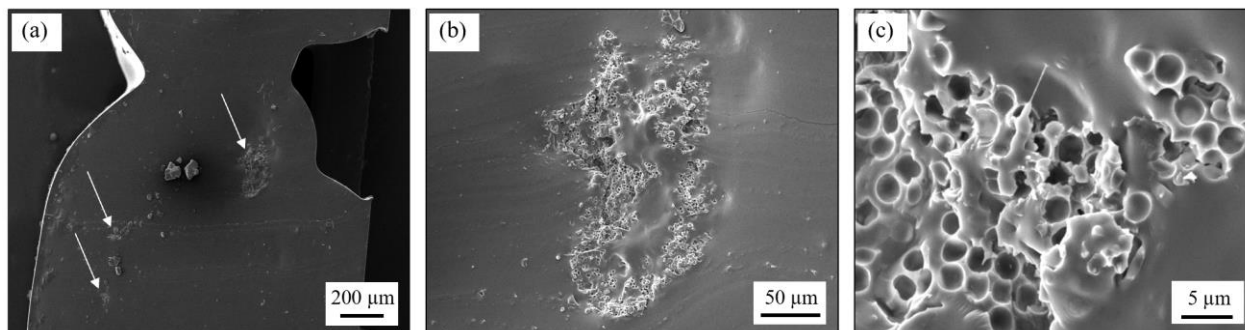


Figure 2.14. SEM images of 3D printed PDMS/PFs lattice specimen showing a cluster of hollow spheres within the bulk material.

2.4 Conclusion

The dispersion polymerization method used to create hollow polysiloxane microspheres lends itself towards becoming a large-scale process because of its simple design, feasibility of batch polymerization, and straightforward sol-gel process. Chemically synthesizing the large,

uniform core polystyrene microspheres was the most challenging task to overcome because it is presently associated to advances in polymer chemistry that requires more understanding than what is currently comprehended. Thus, these uniform microspheres that are easily incorporated into the polymer matrix for 3D printed structures are to be further characterized and optimized for future applications in industrial, biomedical, and nuclear fields. The templated spheres achieved ultimately surpassed our goal of 5 μm with a coefficient of variation $<10\%$, deeming these particles as monodisperse.

However, this work is an on-going investigation to determine both the mechanical and thermal properties of the hollow polysiloxane microspheres themselves as well as the PDMS/HS 3D printed samples. These findings should reveal the effect shell wall thickness, %inclusions of hollow spheres, testing temperature, and polymer properties have on the final oligomeric printed structures.

Chapter 3: Additive Manufacturing of Polyetheretherketone for High Temperature Applications

3.1 Introduction

The desire to substitute conventional materials using polymers is increasing due to the advanced capabilities polymers produce, specifically those in the PAEK family. High performance PAEK (Polyaryletherketone) is a family of semi-crystalline thermoplastics with high temperature stability and high mechanical strength. These thermoplastics are suitable for materials required to sustain extreme environments for industrial, aerospace, and medical applications [31,32]. Within the various subgroups of the PAEK family is PEEK (Polyether ether ketone).

The chemical structure in PEEK has a remarkably high molecular weight and long chain characteristic for superior impact resistance and polymer bond strength due to increased entanglement in comparison to other polymers. Additionally, PEEK's molecular structure is composed of polar carbonyl groups which serve to increase the polymers stability at high temperatures exceeding 200°C. PEEK also has high resistance to chemical and radiation damage, is compatible with many reinforcing additives (such as glass and carbon fiber), and has superior strength to many metals.

Currently, the processes in which PEEK is manufactured is through injection molding, extrusion, compression molding, and so on [33]. The greatest obstacle these manufacturing methods impose is the need of heating at very high temperatures, particularly detrimental in plastic injection molding since the process temperature of PEEK exceeds the range at which most injection molding machines can operate. In addition to the temperature obstacle,

dimensional freedom without the use of machining is limited and reliant on the geometry of the molds being used.

PEEK was printed using commercially available Funmat HT (Intamsys) equipped with a high temperature-controlled chamber up to 90°C and max temperatures of the hotend extruder and bed to be 450°C and 160°C, respectively. The objective of printing PEEK using this 3D printing technology was to investigate the fabrication and thermal post-processing of the physical, mechanical, and thermal-mechanical properties of this semi-crystalline polymer.

3.1.1 Additive Manufacturing of PEEK

Commercially available PEEK filament (diameter=1.75 mm, Intamsys) was used for the fabrication of dogbone specimens using the Intamsys Funmat HT 3D printer. The printing parameters found in Table 3.1 produced specimens with $\geq 85\%$ theoretical density of pure PEEK (1.32 g/cm³) [33]. The generic raster angle of +45°/-45° was selected to produce these preliminary findings, however, different raster angles such as 0°/90° and 30°/60° orientations are of interest to determine their impact on mechanical properties [34]. The glass build plate provided was coated on one side with a ceramic finish where the dogbones (Type IV) could be printed without the use of adhesive where constant monitoring of the print and increase in build plate temperature were needed. Although this absence of adhesive could provide neat PEEK samples for testing, the specimens were more susceptible to lifting and warping. As a result, a commercial nano-adhesive (Vision Miner) was coated onto the glass substrate which successfully increased adhesion and minimized printing errors.

Table 3.1. *Intamsys Funmat HT FDM printing parameters of PEEK.*

| <i>Parameter</i> | <i>Value</i> | <i>Unit</i> |
|-----------------------|---------------|-------------|
| Nozzle Temp. | 400 | °C |
| Build Plate Temp. | 150 | °C |
| Chamber Temp. | 90 | °C |
| Print Speed | 15 | mm/s |
| Layer Height | 0.1 | mm |
| Nozzle Inner Diameter | 0.4 | mm |
| Filament Diameter | 1.75 | mm |
| Build Orientation | Z-orientation | (Flat) |
| Infill Pattern | Lines | - |
| Raster | 45 | ° |
| # of Contours | 3 | - |

3.1.2 Crystallinity

PEEK's mechanical properties are greatly influenced by thermal processing, molecular weight, and tacticity [35,36]. However, investigating solely thermal influence on the printed PEEK was viable due to our constraint of purchasing commercial filament rather than fabrication due to the difficulty of solvent casting and extruding homogenous PEEK filament. This thermal post-processing has been shown to affect the crystallinity of a polymer. Crystallinity is the structural order of the molecular chains which produces different mechanical and thermal properties of the polymer. As crystallinity increases, the range of working temperatures, elastic modulus, and ultimate tensile strength typically increase [35]. However, the material characteristically has a loss in toughness due to increased brittleness and different tribological behaviors.

3.1.3 Thermal Post-Processing

Post-processing in the form of annealing or “cold-crystallization” process is a common practice towards increasing the mechanical properties of typical amorphous regions of polyetheretherketone. By heating the amorphous material to a temperature above its minimum

crystallization temperature ($\sim 155^{\circ}\text{C}$), but below its melt temperature ($\sim 340^{\circ}\text{C}$), the crystallization fraction may be increased [36,37]. Dwell time is of lesser significance since much of the crystallization is rapid and occurs during the rate of cooling [35,36,38,39]. The annealing process was executed by inserting two printed PEEK dogbones on an alumina crucible into a tube furnace (OTF-1200X-S-NT, MTI Corporation) with an inflow of air. The annealing temperature profile can be seen in Figure 3.1. where initial temperatures tested were 200°C and 220°C which had shown to be a good initial point for increasing crystallinity up to 35% according to literature [35]. The dwell temperature was suggested to be 1 hour/mm in thickness (4 mm) of the printed specimens and the cooling rate was 1 hour/ 10°C to cool to 140°C [40]. Afterward, the specimens were let to cool to room temperature at $10^{\circ}\text{C}/\text{min}$.

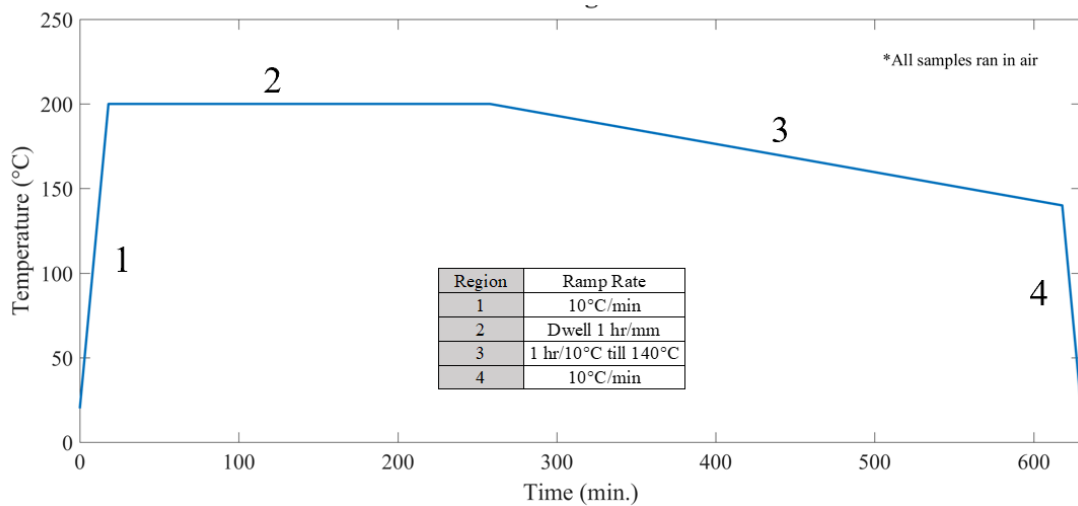


Figure 3.1. Annealing profile of printed PEEK dogbones.

An experimental error was found when using the tube furnace where the temperature read from the thermocouple was discovered to be significantly lower than the desired temperature. For instance, the 200°C and 225°C ran on two pairs of PEEK dogbones were in fact held at roughly 150°C and 175°C , respectively. As a result, the cooling rate of those specimens ran at 150°C to reach 140°C over a 6-hour period was $0.028^{\circ}\text{C}/\text{min}$. This consideration is also true

where samples were experimentally held at 175°C and cooled to 140°C for 8.5 hours (cooling rate: 0.069°C/min.). These samples were still investigated regarding their mechanical and thermal properties. Annealing at 200°C and 225°C was redone by overshooting the set temperature of the tube furnace by roughly 50°C where the actual temperature inside the quartz tube was measured using a thermocouple. This offset temperature of the tube furnace was also affected by the air inflow.

3.2 Results

3.2.1 Mechanical Testing

Tensile testing of 3D printed specimens (Type IV) was executed following ASTM D638 using an Intron 5866 testing machine equipped with a video extensometer. The specimens were tested at room temperature with a 10 kN-load cell and a strain rate of 5 mm/min. Typical tensile strength and elastic modulus of molded semi-crystalline PEEK performed by ISO 527 testing standards are 100 MPa and 4 GPa, respectively [33]. Figure 3.2 and Figure 3.3 show the averaged mechanical properties with error bars of standard deviation for the PEEK samples as a function of their thermal post-processing. Ultimate tensile strength (UTS) of PEEK specimens ranged from 75.8 MPa to 92.1 MPa, roughly 84% theoretical strength of PEEK. This overall loss in strength could be attributed to the printing processes where losses in density resulting from printing speed and layer height produced porosity. The printing direction also influences the mechanical properties. A linear trend of ultimate tensile stress was expected, however, specimens annealed at 150°C were found to have the greatest strength. This could be attributed to having the slowest cooling rate and closest dwell temperature to the glass transition temperature [35,38]. However, the specimens annealed at 200°C produced the greatest Young's modulus followed by those processed at 150°C. This could be a result of different isothermal

crystallization growth for specimens treated at 200°C rather than 150°C that permit the macromolecular chains within this crystalline region to resist elastic deformation [35]. In both instances, samples that were not introduced to a thermal post-processing had the lowest strength (75.8 MPa) and Young's modulus (3.2 GPa) values. Each data set for these preliminary mechanical testing was comprised of only two samples; therefore, more data is required for solidifying these findings.

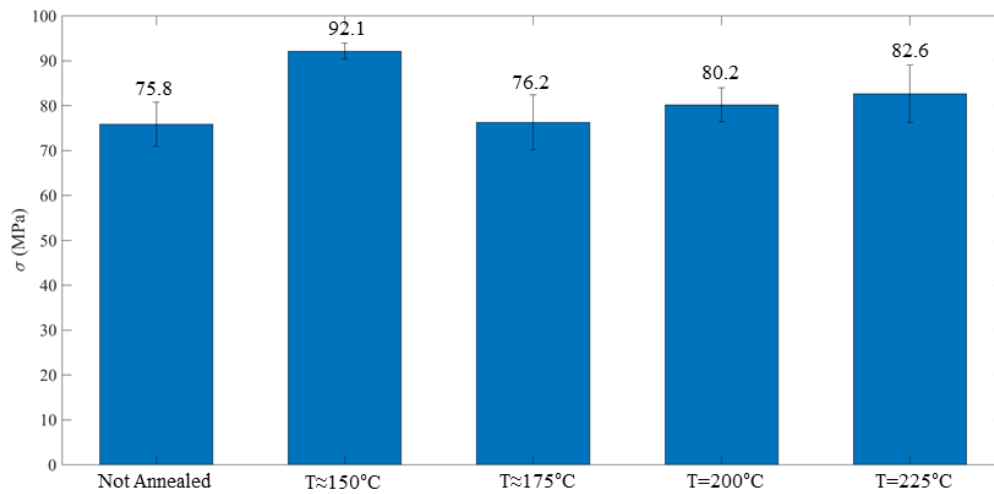


Figure 3.2. Ultimate tensile stress of printed PEEK dogbones under five different post-processing conditions.

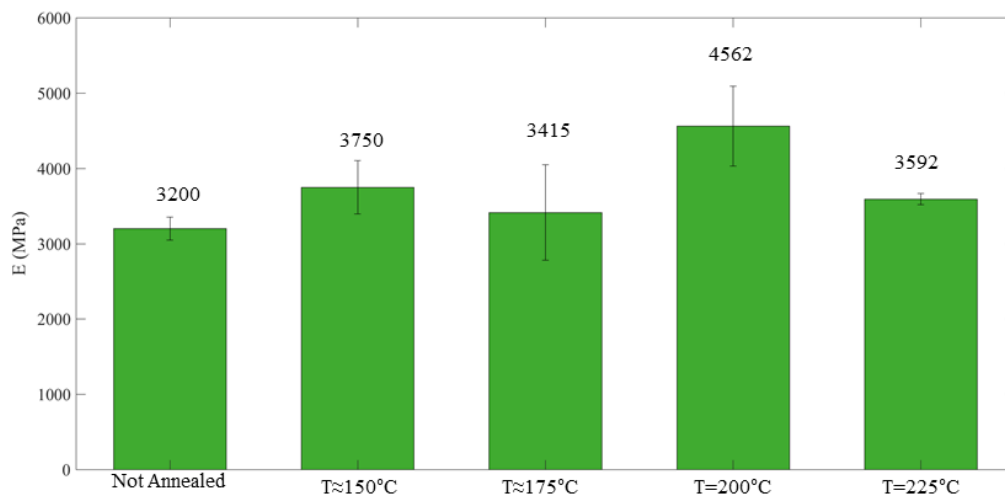


Figure 3.3. Young's modulus of printed PEEK dogbones under five different post-processing conditions.

The stress-strain curve of the 3D printed specimens for the five sample sets are shown in Figure 3.4. Here, variations can be seen between individual samples that were annealed together as well as comparisons as annealing temperatures differentiated. The specimens annealed at 150°C individually had the greatest stress and strain of 92.1 MPa and 0.096 mm mm⁻¹ for specimen 4 and specimen 3, respectively. Further generation of data points may require investigations into different modes of fractures such as crazing, porosity, printing parameters, and so on by considering the morphology of the specimens after break.

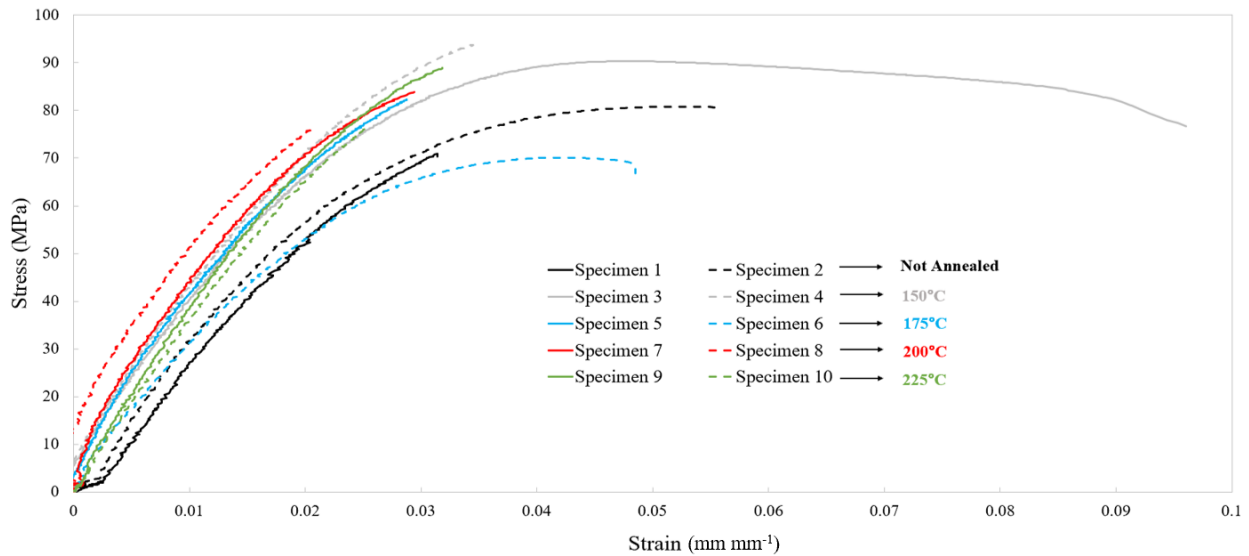


Figure 3.4. Stress-strain curve of PEEK specimen sets under five different post-processing conditions.

3.2.2 Degree of Crystallinity

Crystallinity can be investigated by several different methods such as SAXS, WAXS, differential scanning calorimetry (DSC), TEM, and density measurements [36]. For the availability and feasibility of quantifying the physical properties of the annealed specimens, DSC was used for this study to measure the glass transition temperature (T_g), melting temperature (T_m), and change in enthalpy of the printed PEEK. Note: only one sample of each not annealed, annealed at 150°C, and annealed at 175°C specimens were investigated due to time constraint

and more studies of determining crystallization affected by the annealing process are required. These measurements were taken by cutting from the fracture point of the core PEEK material after tensile tests were performed. This collection point was crucial to avoid producing any additional variation in data due to differences in the outer layer and core crystallinity. It is well known that outer layer (regions closer to the contour lines) experience a more rapid cooling rate which reduces the degree of crystallinity. Glass transition temperature of a polymer is the point in which the polymer shifts from amorphous to a more linear-elastic structure which is indicated as the onset temperature of the first endothermic slope as seen in Figure 3.6 to be approximately between 150°C-165°C. Dynamic mechanical analysis (DMA 850 TA Instruments) was also used to validate the T_g of a 60 x 10 x 3 mm (l x w x h) unannealed PEEK specimen where thermomechanical affects are shown. This test was performed by using a dual cantilever beam employing a 20 μ m amplitude, 1 Hz frequency, and a ramp rate of 3°C/min. to reach 320°C. This dampening behavior of the material as a function of the linear temperature increase and cyclic loading show how well the PEEK sample performs at dissipating energy [41]. Figure 3.5 indicates the T_g region to be between 150°C-163°C at the onset of storage modulus (E') and the peak of $\text{Tan } \delta$, respectively [42].

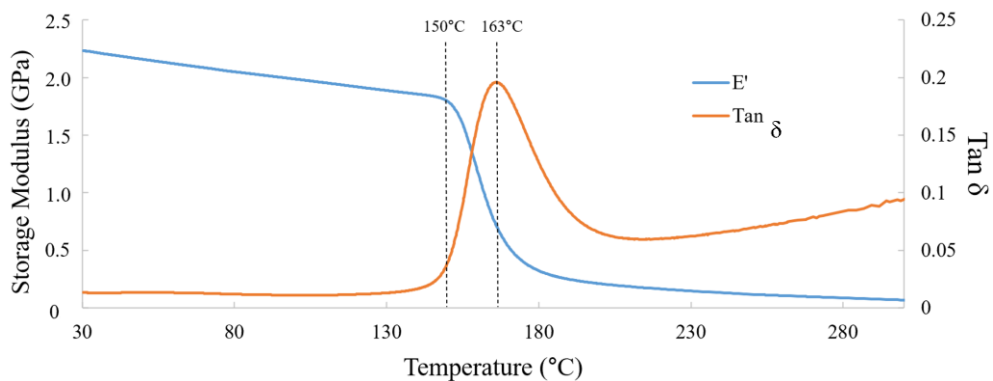


Figure 3.5. DMA of printed PEEK from 30°C to 320°C.

To calculate percent crystallinity, Eq. 3.1 was used where the relationship between the ratio of the melting endotherm during the 2nd heating cycle and enthalpy of fusion of a theoretical 100% crystalline PEEK sample (130 J/g) can be seen:

$$\%C = \left(\frac{\Delta H_c}{\Delta H_t} \right) \times 100 \quad (3.1)$$

Here, ΔH_c denotes the experimental value of the melt endotherm and ΔH_t denotes the theoretical value of PEEK enthalpy [37]. Assuming the specimens annealed at 150°C must have a higher

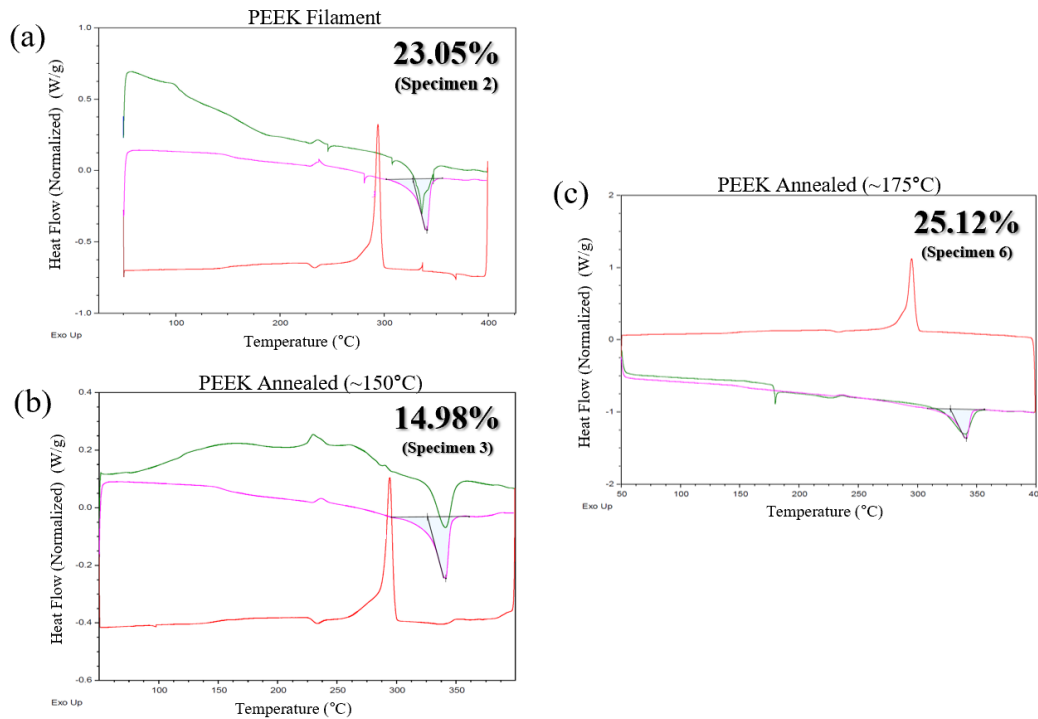


Figure 3.6. DSC curves denoting the percent crystallinity of printed PEEK with different thermal post-processing of (a) unannealed, (b) annealed at 150°C, and (c) annealed at 175°C correlating to samples from the stress-strain curve.

crystallinity due to their greatest average ultimate tensile strength, the DSC curves shown in Figure 3.6 could not completely validate this initial claim. Specimen 3 had a lower crystallinity fraction (14.98%) as opposed to the unannealed sample but allowed the sample to have the greatest % elongation. Although specimen 6 which was annealed at 175°C provided a slightly higher crystallinity fraction than the unannealed specimen, it had less strength than its

counterpart. Contributing factors for the opposing findings between crystallinity percentage and strength as well as differences between individual specimens processed together could be a result of: (1) tensile test slippage from the fixture grips which may have induced premature fracture or (2) non-uniform heating of specimens when annealed. Fractography on tensile specimens could be done using SEM to investigate the growth of spherulites or polymer deformation to give insight on morphology. Also, detection of crazing would be expected in the amorphous PEEK regions of specimens while a more semi-crystalline polymer would have a shear deformation mechanism [43].

3.2.3 Sulfonation

Currently, advancements in functionalizing this high-temperature polymer to further alter the properties of PEEK for more applications is of high interest. The sulfonation of PEEK is a chemical process where you introduce a sulfonic acid group into the polymer backbone which increases its conductivity while maintaining PEEK's chemical inertness and thermal stability. This semiconductive sulfonated PEEK (SPEEK) polymer could be used as a matrix for high temperature piezoelectric filament. By increasing the conductivity, it would allow promote higher electrical response from piezoceramic inclusions within the matrix. Typically, these piezoelectric ceramics such as barium titanate and lithium niobate are included into polymers with relatively low melting temperature ($<200^{\circ}\text{C}$). However, SPEEK could widen the range of operable 3D printed piezoelectric sensors for extreme environments.

Primarily, this semiconductive material is desired for polymer electrolyte membrane fuel cells (PEM-FC) found in systems such as space vehicles and submarines [44]. These fuel cells can convert the chemical energy of a fuel (typically hydrogen and methanol) directly into electrical energy with relatively high efficiency as well as for their adaptable size and relatively

low operating temperature. Nafion is commonly used as this matrix because it has proton-exchanging capabilities, however, it is only operable up to roughly 100°C for current systems [45]. Therefore, replacing such materials with PEEK increases operating temperatures which allows fuel cells to be implemented in high-temperature environments.

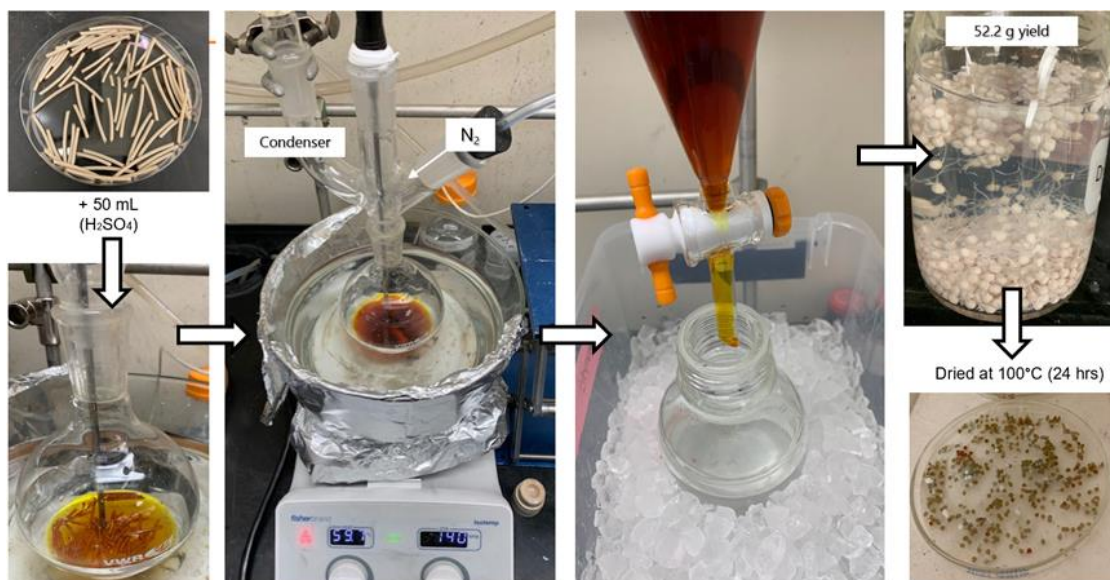


Figure 3.7. *Experimental setup for sulfonating PEEK material.*

The rather extensive process followed to sulfonate PEEK is shown in Figure 3.7 where 5 g of PEEK (VITREX-450P) was added to sulfuric acid for 6 hours at 60°C; temperature and soak time change the degree of sulfonation. (Note: PEEK filament is shown in Figure 3.7, however, powder minimized clumping of the polymer material and dissolved more efficiently). Then, the reaction was terminated by precipitating it into cold water. The material was soaked overnight then washed until the pH was neutral. Lastly, the SPEEK was dried in an oven at 100°C for 24 hrs. Thermogravimetric analysis (TGA) indicated in Figure 3.8 reveals the difference in weight loss between PEEK and SPEEK where PEEK has one distinct region with an onset degradation of the polymer backbone of 543°C but SPEEK has three regions; the first being the removal of any residual water or solvent absorbed by the relatively hydrophilic

polymer, followed by the desulfonation region, and lastly the polymer backbone decomposition. The backbone degradation temperature of SPEEK decreased to 474°C compared to 543°C of neat PEEK, but the materials high temperature polymer classification remains [46,47].

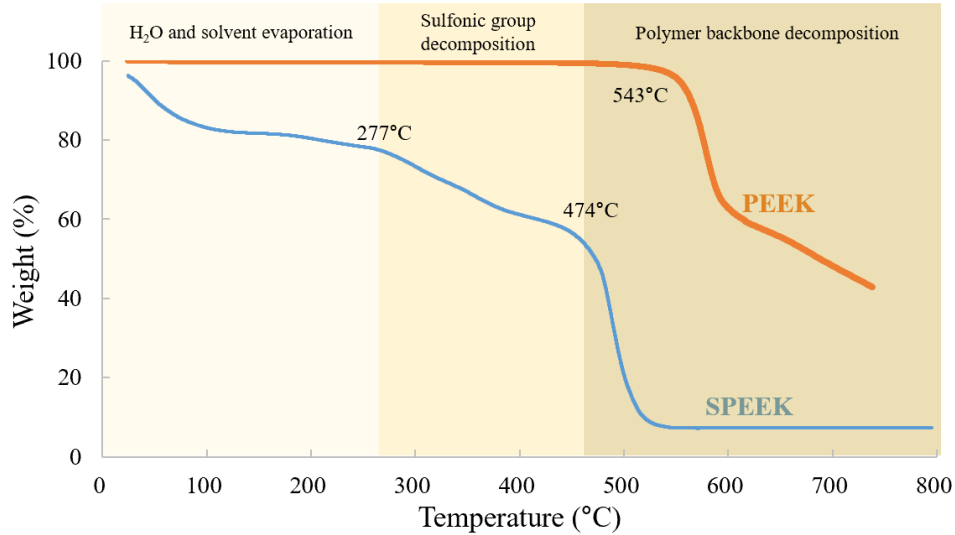


Figure 3.8. TGA curves of PEEK and SPEEK with a heating rate of $10^{\circ}\text{C min}^{-1}$.

3.3 Conclusion

This work attempted to investigate the degree of altered mechanical and thermal properties based on the annealing of PEEK specimens that were 3D printed using a material extrusion process. The specimens annealed close to PEEK’s glass transition temperature at 150°C with the slowest cooling rate of $0.028^{\circ}\text{C/min}$. to reach 140°C produced the specimens with the greatest tensile strength (92.1 MPa) that is relatively close to theoretical mechanical properties of molded PEEK. However, the specimens with a higher dwell temperature of 200°C and cooled at a rate of $0.167^{\circ}\text{C/min}$. to reach 140°C had the highest Young’s modulus of 4562 MPa. Although it is expected to have a linear trend with corresponding mechanical properties attributed to one set of samples, these differences in tensile stress and Young’s modulus are caused by several factors such as: (1) printing parameters, (2) relaxation of internal stresses due

to annealing process, and (3) polymer morphology. The crystallinity of the best performing specimens could not be fully determined based on the lack of DSC testing and samples for comparative data. However, it can be inferred that there is a possibility to tune mechanical properties where the specimens annealed at 150°C could lead to developing PEEK samples with both increased strength and toughness for different applications.

For sulfonated PEEK, preliminary experimentation was conducted to determine the feasibility of utilizing the semiconductive polymer as the matrix material for high temperature piezoelectric 3D printed composites. Optimizing the degree of sulfonation with respect to the loss in thermal properties is needed to continue onto the formation of the SPEEK membrane. This membrane will be used in a solvent casting method where a piezoelectric ceramic with a high curie temperature capable of withstanding 400°C for printing will be incorporated into the mixture. Casting of these high temperature nanocomposites are to be tested to determine their initial functional properties and degree of sulfonation. Lastly, forming the nanocomposite filament using a filament extruder and utilizing it to study the effect 3D printing has on the functional properties will be conducted.

Chapter 4: Multifunctional Sensing Using 3D Printed CNTs/BTO/PVDF Nanocomposites

4.1 Introduction and Background

The feasibility of printing functional structures with tailored properties could lead to the rapid manufacturing of composite materials for multifunctional sensing applications. The functionality of such structures derives from the piezoelectric effect. Piezoelectric materials are of high interest due to their inherent ability to produce an electrical output from an applied mechanical force and vice-versa (inverse piezoelectric effect). More specifically, materials such as polyvinylidene fluoride (PVDF) and barium titanate (BTO) are well-known smart materials used as piezo-/di-electric devices for sensor and energy storage due to their unique characteristics. PVDF was selected as the 3D printed composite matrix due to its acute material properties including: 1) lightweight, 2) thermally stable and chemically resistant, 3) high dielectric breakdown strength, 4) and mechanically durable, tough, and flexible. Although PVDF provides great mechanical properties as the matrix, it has a low piezoelectric coefficient ($d_{33} \approx 33$ pC/N). Therefore, introducing a ceramic that has a high piezoelectric effect combined with the high flexibility and toughness of the PVDF polymer is of interest. There are many different available piezoelectric ceramics (i.e. PZT, LiNbO, ZnO, etc.), however, BTO was selected due to its relatively high d_{33} (149 pC/N), high curie temperature, and lead-free composition. The composite could be used for a variety of applications such as sensors, actuators, capacitor, energy harvesting, structural health monitoring for electronic, biomedical, aerospace, and transportation fields.

Although the dispersed ceramic increases the electrical performance of the composite, further improvement of the piezo-/di-electric performance as well as tensile strength was employed by the introduction of organic fillers such as carbon fiber, carbon nanotubes (CNTs),

and carbon black. These organic fillers have been extensively investigated by incorporating them in polymer composites [48-52]. Researchers investigated other areas of CNT-based strain sensors using their piezo-capacitive and resistive effects on highly stretchable elastomer substrate or in a polymer matrix for robotics, structural health monitoring, human skin, interactive electronics, smart clothing, and strain gauge [53-58]. Strain sensing of polymer CNTs nanocomposites is based on the electrical variations induced by external stresses, destruction of the interconnected CNTs' conductive networks, and changes in resistance due to the varying distances between CNTs [55]. These CNTs were introduced into the matrix to serve as stretchable electrodes. Also, to mix and enhance the response of polymer materials tested within limited lower strain parameters. Ultimately, these CNTs were utilized as the structural material itself as the intrinsic sensor which is also referred to as self-sensing. As a result, advantages of multi-functionality, low-cost, high durability, large sensing volume, and the absence of mechanical property degradation are produced [55,59].

4.2 Motivation of FDM Printing Multifunctional Sensors

Recently, it has been proved that coupling the two processes of filament extrusion and fused-deposition modeling (FDM) 3D printing could provide a homogeneous dispersion of BTO and possibly other additives in PVDF. Additionally, these techniques helped in alleviating agglomerations and the removal of voids and cracks [60]. The 3D printed piezo-/di-electric nanocomposites using FDM 3D printing technique was studied to improve both their electrical and mechanical performances by integrating polymer with piezo-/di-electric ceramics. This printing technique could provide great improvements for physical and mechanical properties including piezoelectric coupling coefficient, relative dielectric permittivity, ultimate stress, and ultimate strain [60-63]. With the high toughness of the 3D printed multifunctional

nanocomposites, it can be potentially used as an intrinsic self-powered pressure sensor and facilitate energy storage capabilities [60,63]. By utilizing the characteristics of CNTs and BTO nanoparticles in a PVDF matrix coupled with the increased filament matrix homogeneity resulting from the FDM 3D printing technique [63], the sensing capabilities regarding strain and temperature changes were feasible. To do this, capacitance-based responses in the printed specimens under strain and temperature changes were considered.

Furthermore, this study identifies the impact of filler content of BTO and CNTs below percolation threshold on electrical property changes of FDM 3D printed CNTs/BTO/PVDF nanocomposites for multifunctional temperature and strain sensing applications. Additionally, tensile testing was executed to characterize tensile stress and strain on each sample for their mechanical property.

4.3 Methodology

For the fabrication of filaments that produced a continuous CNTs/BTO/PVDF nanocomposite through the use of 3D printing, the following materials were used: PVDF powder ($M_w = 534,000$, Sigma-Aldrich), BT powder (700 nm, Inframat), multi-walled carbon nanotubes (CNTs) powder (diameter: 8-15 nm, length: 10-50 mm, Cheaptubes), and N-Dimethylformamide solvent (DMF, OmniSolv). With respect to varying BTO nanoparticle sizes, BTO powder with 700 nm nanoparticle size withholds its maximum capacitance at 1 kHz in greater loading systems [64,65]. The solvent casting method is shown in Figure 4.1 beginning with a uniformly dispersed mixture of BTO and CNTs in DMF solvent then incorporating sonication for 30 min. The addition of 1:10 weight ratio of PVDF powder was included after the sonication and the total mixture was placed in a water bath for 10-15 min, or until the PVDF powder visibly dissolved at 80°C. Ultra-sonication (Branson Sonifier 450) was applied to the solution for 15 min. that

allowed BTO and CNTs clusters to be alleviated. Lastly, the nanocomposite substrate was formed by evaporating DMF solvent once pouring the solution out into a glass substrate and placed to be heated on a hot plate for 12 h at 80°C.



Figure 4.1. Solvent casting method of forming CNTs/BTO/PVDF nanocomposites.

4.3.1 Additive Manufacturing of Nanocomposites

The resultant dried solvent casted nanocomposite sheets were cut and fed into a single-screw Filabot extruder at 205°C. The extruded filament was cut and re-fed into the extruder up to three times to promote homogeneous distribution of material using a single-screw Filabot extruder. The nanocomposite filament was then used to 3D print a thick film by using an FDM 3D printer (Lulzbot Taz 5) for multifunctional sensing capabilities. This filament extrusion and 3D printing processes are proved in the literature to provide better dispersion of nanoparticles in the matrix than solvent-casting alone, therefore enhancing piezoelectric and mechanical properties.

4.3.2 Characterization

The morphology of the 3D printed nanocomposite samples was observed using a scanning electron microscopy (SEM) while x-ray diffraction (XRD) was performed to characterize crystallinity using CuK α radiation on a D8 Discover diffractometer (Bruker). For the nanocomposite films printed, dielectric property was characterized using electrodes in the form

of conductive silver paint (SPI supplies) on opposing surfaces. An LCR meter (1920 Precision) was utilized to connect the electrodes of each individual 3D printed nanocomposites for considering the capacitance of each sample.

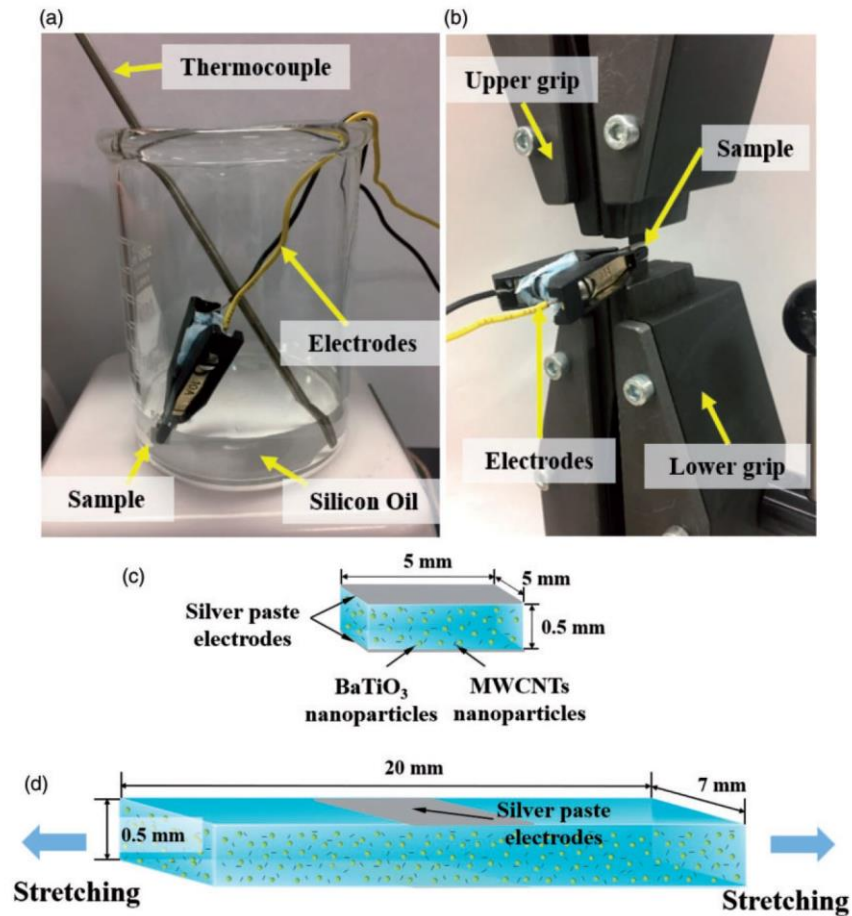


Figure 4.2. Experimental setup and sample preparation for testing multifunctional sensing capabilities.

4.3.3 Multifunctional Testing

Temperature testing was carried out by submerging the sample in a silicon oil and connecting the silver electrodes. Using a hot plate, each film was cut into a 5x5x0.5mm dimension and tested from 25 to 150°C with incrementing temperatures of 25°C for a total of six data points as shown in Figure 4.2 (a) and (c). Each sample was then tested for capacitance value. Strain sensing capabilities were proved from painting 5x7mm electrodes on corresponding

sides of the films shown in Figure 4.2 (b) and (d) and a displacement rate of 3 mm/min. was used for tensile testing (ADMET MTESTQuattro eXpert 5600 series). Recordings of the capacitance were taken at each 1mm displacement with a frequency of 1 kHz [66]. Note that five samples were tested in each test under same condition and average was taken to determine the following results.

4.4 Results

4.4.1 Multifunctional Property Testing: Temperature Sensing

To characterize temperature sensibility of the 3D printed nanocomposites, 3D printed films with varying BTO and CNTs contents in PVDF matrix were tested at elevated temperature in the silicon oil environment. As shown in Figure 4.3, all nanocomposites films show an increasing trend of the capacitance at 1 kHz as temperature elevates from 25 to 150°C. All films started deforming and melting at temperatures above 150°C. In Figure 4.3(a), pure PVDF film ($T_m = 177^\circ\text{C}$) shows a slightly changing rate in the capacitance than films with BTO particles since molecular mobility of pure PVDF is significantly promoted with increasing temperature. At low temperature, PVDF molecules have difficulty in responding to applied electrical field due to poor molecular mobility. At high temperature, the mobility is significantly improved but still restricted by hydrogen bonding [67,68].

In theory, BTO has a Curie temperature around 125°C where the capacitance suddenly depletes [69]. However, this Curie point drop for BTO particles is absent in the PVDF matrix when temperature increases. It was found that there are some possibilities for causing the absence of BTO's Curie peak: (1) for ultra-fine BTO particles (<1 μm), there is an increasingly important surface charge effect where the polarization of the tetragonal structure is locked which allows temperatures to persist to higher temperatures, [70-73] (2) large number of defects are

caused by O_2^- deficiency in perovskite structure, however, F^- from PVDF may substitute some of the O_2^- vacancy or loosely coupled with Ti ion in BTO so that these bonding may alter the BTO phase transformation [73,74] and (3) possibly diffuse phase transition in BTO [75,76]. At high temperatures, generally BTO particles retain better polarization, therefore, the changing rate in capacitance rises as increased amounts of BTO particles are added to the PVDF matrix.

Additionally, it was found that the addition of CNTs fillers led to a much higher capacitance at room temperature due to the following reasons: (1) according to the microcapacitor model, each two adjacent CNTs can locally serve as two electrodes among ceramic nanoparticles and polymer matrix [50], (2) CNT nanoparticles have ultra-high surface area that can induce an ultra-high polarization density, resulting in an increased capacitance [77], and (3) both CNTs and BTO strongly tend to entangle into agglomerates; however, when used together, the CNTs and BTO nanoparticles interact and reduce agglomeration of the CNTs networks in the polymer matrix so that this mixture leads to an increased capacitance level [49]. Under elevating temperatures up to 150°C , the changing rate in the capacitance increases as more CNTs are introduced in the BTO/PVDF system. This is because the increased polarization of BTO nanoparticles is amplified between locally distributed two adjacent CNTs electrodes. Overall, the sample among the different variations of BTO and CNTs found in Figure 4.3(e), 1.7 wt.% CNT/60 wt.% BTO showed the highest changing rate in the capacitance which implies the highest temperature sensibility.

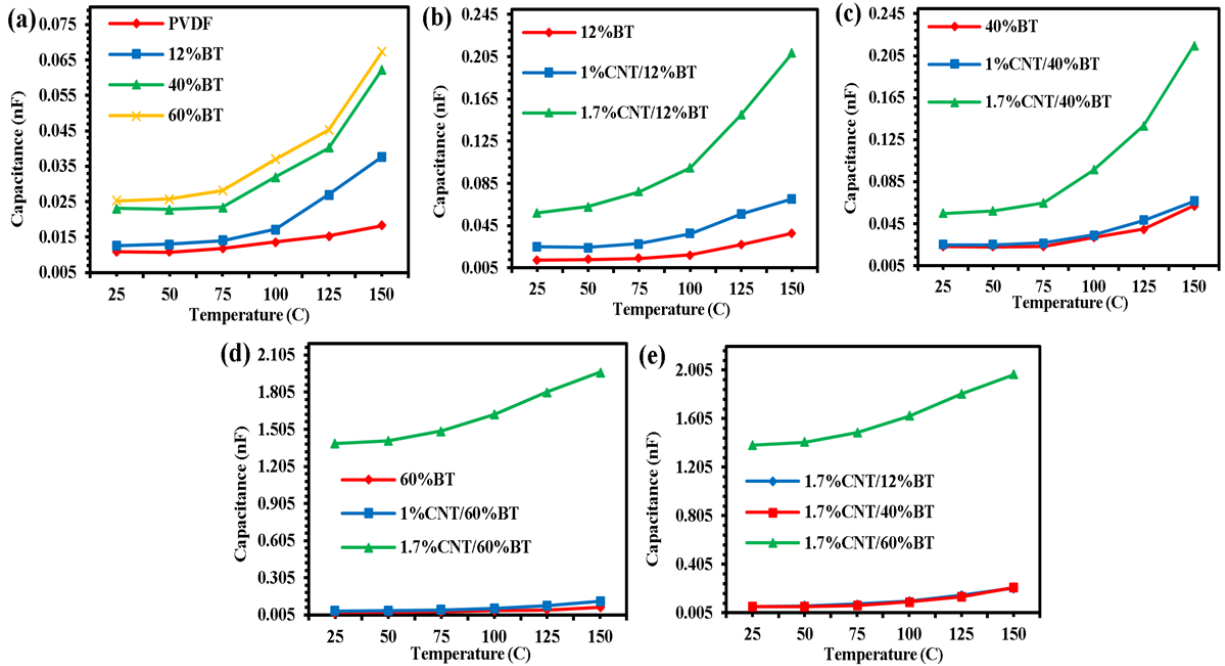


Figure 4.3. Temperature sensing as a function of measured capacitance for various inclusions of CNTs and BTO.

4.4.2 Multifunctional Property Testing: Stress-Strain

The influence of BTO and CNTs nanoparticles on the mechanical properties of PVDF matrix was examined by analyzing the tensile behavior of the 3D printed CNTs/BTO/PVDF nanocomposites films. Figure 4.4(a) shows a stress–strain curve for each sample with varying weight percentages of CNTs and BTO tested at the strain rate of 3 mm/min. In general, low inclusion content means that inclusion increases tensile strength because the polymer chains within the amorphous regions are restricted [78,79]. However, in a high loading system, the tensile strength decreases as inclusion content increases as shown in Figure 4.4(b). Exceptionally, there is an increase in the ultimate tensile strength (UTS) for BTO/PVDF nanocomposites without CNTs at 40wt.% BTO. Although it is observed that 12 wt.% BTO showed higher UTS than 40wt.% BTO around 50% strain, the 40wt.% BTO breaks at a higher tensile strength. This occurs because tensile strength right before rupture directs the polymer

chains to be oriented and aligned along the tensile load direction which increases the strength and stiffness of the polymer in the stretching direction, also known as strain hardening [48]. During the rupture moment, BTO agglomerates can act as reinforcements in the polymer matrix. The more BTO content that is in the polymer matrix, the higher UTS can occur before the rupture.

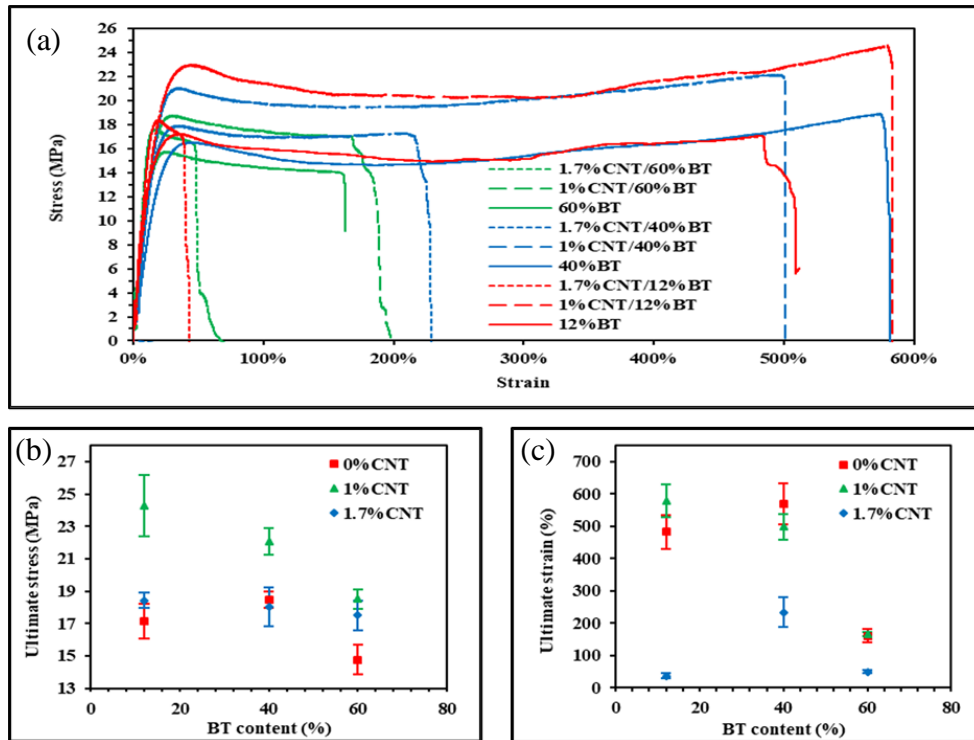


Figure 4.4. Stress-strain curve of CNTs/BTO/PVDF nanocomposites and their correlating (b) ultimate stress and (c) ultimate strain.

As introducing more CNTs content in BTO/PVDF nanocomposites, significant improvement in UTS is observed at 1 wt.% CNTs (24.2 MPa) and then it diminishes at 1.7 wt.% CNTs (18.4 MPa). Similarly, UTS decreases as BTO content increases. This relationship can be attributed by the following reasons: (1) inclusions of BTO and CNTs are more likely to agglomerate and be heterogeneously distributed in higher loading systems have been shown where BTO agglomerates and CNTs clusters increase in higher inclusion content [62,80] and (2)

voids and micro-cracks can be created during the fabrication process and increased with higher filler content [62,81,82]. This means that the total amount of bonding of PVDF molecular chains was decreased [62]. Therefore, these agglomerates and defects led to the degradation of the tensile strength after 12wt.% BTO and 1wt.% CNTs.

Higher failure strains are observed around 550% at 12 and 40 wt.% BTO with no CNTs or 1 wt.% CNTs. It is assumed that increased inclusion helped prevent crack propagation. However, at content loading of 60 wt.% BTO and 1.7 wt.% CNTs, the failure strains are abruptly diminished because the 3D printed nanocomposites became brittle due to reasons mentioned above. Among the 3D printed nanocomposites, it is observed that 1 wt.% CNTs/12 wt.% BTO/PVDF shows the highest mechanical toughness (24.2 MPa and 579%).

4.5 Conclusion

In this study, CNTs/BTO/PVDF nanocomposites were fabricated using FDM 3D printing process for temperature and strain sensing applications. It is found that the capacitance property of the 3D printed nanocomposites can be utilized in sensing the changes of temperature and strain. The highest sensibility for temperature is observed in nanocomposites containing 1.7 wt.% CNTs/60 wt.% BTO/PVDF which are the maximum loading for BTO and CNTs percolation threshold. The highest sensibility for strain is observed in nanocomposites containing 1 wt.% CNTs/12 wt.% BTO/PVDF. The nanocomposites above 1 wt.% CNTs resulted in the degradation of the changing rate in the capacitance. This degradation was because the CNT cluster effectively destructs capacitance as the strain is induced. It is observed that the addition of more than 12 wt.% of BTO particles degrades the changing rate in the capacitance because Poisson's ratio becomes lower as the BTO content increases at a higher loading system. The combination between CNTs and BTO inclusions contributes to a high changing rate in the

capacitance when it comes to the temperature and strain changes. The superior mechanical performance is observed in nanocomposites containing 1wt.%CNTs/12wt.%BTO/PVDF showing 24.2MPa and 579% for mechanical stress and strain, respectively. These improved mechanical properties stem from CNTs and BTO reinforcements. However, ultimate tensile strength started decreasing after 1 wt.% CNTs and 12 wt.% BTO and failure strain after 1 wt.% CNTs and 40 wt.% BTO. Ultimately, this study demonstrated the feasibility of producing sensors with tunable properties for massive production.

Chapter 5: Summary of Research and Future Work

5.1 Conclusions

These three topics of work demonstrated different methods of utilizing polymers for additive manufacturing processes that are useful for a variety of applications. In the primary chapter, a chemical synthesis technique for polymer structures demonstrated the complexity and importance of material development from the initial molecular level. Hollow polysiloxane microspheres greater than 5 μm were successfully synthesized with uniform particle size to be included into a PDMS matrix. Each modification in the reaction for core formation provided further advancements in understanding the effect of reagent concentrations, reaction temperature, and polymerization kinetics. Core-shell formations using the hydrolysis-condensation reaction of MTMS followed by thermal processing to remove the PS core were validated by FTIR, TGA, and SEM studies. After these pore formers were included into the PDMS matrix to 3D print lattice structures via direct write, the cross-section of a single strut under SEM showed these polysiloxane microspheres retained their geometry and were in fact hollow. In general, this process of chemically synthesizing polysiloxane pore formers is shown to be a well-suited investigation for future large-scaled production of monodisperse microspheres.

The subsequent chapter first highlighted the effect thermal post-processing had on 3D printed PEEK mechanical properties. Although 3D printing of this high temperature polymer allows for the development of complex geometries, loss in density and formation of internal stresses decreases the mechanical performance of the material. Therefore, annealing has been shown to be a method of alleviating these internal stresses whilst increasing the crystallinity of the semi-crystalline polymer which increases the strength and Young's modulus. As anticipated, thermal post-processing showed to increase the overall mechanical performance of 3D printed

PEEK compared to the unannealed specimens. However, discrepancies arose when specimens annealed with a dwell temperature of 150°C with a cooling rate of 0.028°C/min. to reach 140°C produced the greatest ultimate tensile stress of 92.1 MPa; those that had a higher dwell temperature of 200°C and a cooling rate of 0.069°C/min. to reach 140°C produced the greatest Young's modulus of 4562 MPa. There are several potential explanations for this uncorrelation, however, more experimental testing is needed to formulate conclusive statements. Uniquely, if these PEEK specimens can be optimized to increase in both stress and strain, there is a future in developing a thermal post-processing profile that increases these mechanical properties proportionally rather than inversely. Functionalizing PEEK by introducing a sulfonic acid group has been widely developed in manufacturing proton conductive membranes typically for fuel cell applications. However, because sulfonated PEEK (SPEEK) is considered as a semiconductor, it can be used as the matrix material in developing a high temperature piezoelectric filament of additive manufacturing. PEEK powder was successfully sulfonated after being suspended in sulfuric acid for 6 hours at 60°C. Thermogravimetric analysis (TGA) was used for validation where weight loss % were compared between PEEK and SPEEK. The single decrease in weight % for PEEK was found to be the decomposition of the polymer backbone at 543°C while SPEEK had three weight loss % regions: (1) solvent evaporation, (2) desulfonation, and (3) polymer backbone decomposition at 454°C.

In the final chapter, the fabrication of CNTs/BTO/PVDF multifunctional nanocomposite lead-free sensors for mass production were developed and the mechanical and thermal properties were investigated. The capacitance property of the 3D printed nanocomposites was found to be utilized in sensing the changes of temperature and strain. The highest sensibility for temperature were found to be the nanocomposite containing 1.7 wt.% CNTs/60 wt.% BT/PVDF which are

the maximum loading for BT and CNTs percolation threshold. The highest observed sensibility for strain were the 1 wt.% CNTs/12 wt.% BT/PVDF nanocomposite. Mechanical performance was optimal in nanocomposites containing 1 wt.% CNTs/12 wt.%BT/PVDF showing 24.2MPa and 579% for mechanical stress and strain, respectively. These improved mechanical properties are a result of the CNTs and BT reinforcements. However, ultimate tensile strength was shown to decrease after 1 wt.% CNTs and 12 wt.% BT and failure strain after 1 wt.% CNTs and 40 wt.% BT.

In closing, this body of work demonstrated contributions to the chemical synthesis, fabrication, testing, and evaluation of several polymer and polymer nanocomposite structures. Such material development led to contributions not only for polymer chemistry but also for additive manufacturing systems such as direct write and fused deposition modeling. The use of such polymer and polymer-based nanocomposites are baseline contributions for future engineers to further advance different material systems.

5.2 Recommendations for Future Work

This thesis demonstrated fundamental contributions to the synthesis and fabrication of polymer structures used to achieve complex geometries through additive manufacturing. However, further expansions on the work are needed to gather further characterization as well as mechanical and thermal performance regarding the of pore formers within a PDMS matrix. In the case of characterizing large polysiloxane microspheres, it is necessary to investigate the physical properties and shape using mass spectrometry, nanoindentation, solid-state nuclear magnetic resonance (ssNMR), and small-angle x-ray scattering (SAXS). Mass spectroscopy will help determine the polydispersity index and molecular weight of the PS core microspheres. SAXS would provide clear indication of hollow shell wall thickness which will have a direct

effect on the compressive strength and elasticity. Employing the nanoindentation technique will provide a better understanding of the micromechanical properties of the individual polysiloxane spheres. Additionally, ssNMR will provide further insight into the chemical composition of the microspheres that will reveal ways to optimize the growth of the PS core particles. The hollow microspheres also need to be more uniformly distributed within the PDMS matrix for printing where a Thinky Mixer can help alleviate agglomerations and increase homogeneity. Mechanical testing of the PDMS specimens with included pore formers is the necessary crucial step towards identifying the clear effect these synthesizing spheres have on static and dynamic failure, shrinkage, and shock absorption. Thermomechanical properties are also needed to consider different environments the pore formers may be subjected for applications regarding the interests of KCNSC. On-going investigations on further increasing the average diameter of the PS core microspheres through the use of increased temperature, addition of divinylbenzene (DVB), and utilizing a feeding rate to increase uniformity will advance the capabilities of producing a wider range of hollow polysiloxane microspheres. Lastly, developing the dispersion polymerization and sol-gel process to be a large-scale process and identifying ways to reduce cost for this synthesis technique will bring great advancements to the industrial applications. Introducing the use of simulations for such polymerization processes via Monte Carlo simulations would be a good tool to reduce both cost and time for optimizing PS and polysiloxane size and uniformity.

With regards to PEEK, continuation of the printing and mechanical testing of the specimens under the same five thermal post-processing conditions is required. Next, determining the average crystallinity using DSC for each data set will provide a greater correlation between the effect of crystalline growth of the polymer with respect to the mechanical responses. SEM images of the cross-section after fracture will also help in identifying the modes of fracture as

well as the growth characteristics of formed spherulites. Therefore, possibly tuning and increasing the mechanical properties to compete with theoretical values of semi-crystalline PEEK based solely on the annealing profile will advance the 3D printing of complex PEEK geometries. Also, the optimization of printing parameters and thermal post-processing of neat PEEK will enhance the expected electrical response of the high temperature functionalized PEEK filament with piezoceramic inclusions by allowing for greater mechanical loadings. Although the experimental procedure for forming successfully sulfonating PEEK validated by the TGA results have been conducted, this high temperature filament is still in the fundamental phase. Next, the SPEEK pellets formed would need to be solution casted with the addition of piezoelectric ceramic powders having a high curie temperature to produce a homogenous, dried substrate used to form the piezoelectric filament for material extrusion 3D printing. The degree of sulfonation by varying the time and temperature PEEK powder is introduced to sulfuric acid may need to be altered to determine the percolation threshold of the SPEEK matrix. Lastly, electric poling and annealing of SPEEK 3D printed specimens will need to be determined to quantify the mechanical, thermomechanical, and electrical responses.

References

- [1] H. Wang, P. Chen, and X. Zheng, "Hollow permeable polysiloxane capsules: a novel approach for fabrication, guest encapsulation and morphology studies," *Journal of Materials Chemistry*, vol. 14, no. 10, pp. 1648-1651, 2004.
- [2] S. D. Koker, L.J. De Cock, P. R. Gil, W. J. Parak, R. A. Velty, C. Vervaet, J. P. Remon, J. Grooten, and B. G. De Geest, "Polymeric multilayer capsules delivering biotherapeutics," *Advanced Drug Delivery Reviews*, vol. 63, no. 9, pp. 748-761, 2011.
- [3] Z.-Z. Li, S.-A. Xu, L.-X. Wen, F. Liu, A.-Q. Liu, Q. Wang, H.-Y. Sun, W. Yu, and J.-F. Chen, "Controlled release of avermectin from porous hollow silica nanoparticles: Influence of shell thickness on loading efficiency, UV-shielding property and release," *Journal of Controlled Release*, vol. 111, no. 1-2, pp. 81–88, 2006.
- [4] J. Qian, P. Liu, Y. Xiao, Y. Jiang, Y. Cao, X. Ai, and H. Yang, "TiO₂-Coated Multilayered SnO₂Hollow Microspheres for Dye-Sensitized Solar Cells," *Advanced Materials*, vol. 21, no. 36, pp. 3663–3667, 2009.
- [5] L. Zhang and J. Ma, "Processing and characterization of syntactic carbon foams containing hollow carbon microspheres," *Carbon*, vol. 47, no. 6, pp. 1451–1456, 2009.
- [6] R. Arshady, "Suspension, emulsion, and dispersion polymerization: A methodological survey," *Colloid & Polymer Science*, vol. 270, no. 8, pp. 717–732, 1992.
- [7] J.-S. Song, F. Tronc, and M. A. Winnik, "Two-Stage Dispersion Polymerization toward Monodisperse, Controlled Micrometer-Sized Copolymer Particles," *Journal of the American Chemical Society*, vol. 126, no. 21, pp. 6562–6563, 2004.
- [8] G. G. Odian, *Principles of polymerization*, 4th ed. Hoboken, NJ: Wiley-Interscience, 2004.
- [9] F. Li, C. Geng, and Q. Yan, "Growth Kinetics of Monodisperse Polystyrene Microspheres Prepared by Dispersion Polymerization," *Journal of Polymers*, vol. 2013, pp. 1–7, 2013.
- [10] "Polystyrene Polymer," *Polystyrene Polymer - an overview | ScienceDirect Topics*. [Online].
- [11] X. Lu, Z. Xin, "Preparation and Characterization of Micron-Sized Polystyrene/Polysiloxane Core/Shell Particles," *Colloid & Polymer Science*, vol. 284, no. 9, pp.1062-1066, 2006.

- [12] C. J. Brinker, "Hydrolysis and condensation of silicates: Effects on structure," *Journal of Non-Crystalline Solids*, vol. 100, no. 1–3, pp. 31–50, 1988.
- [13] M.-C. Brochier Salon and M. N. Belgacem, "Hydrolysis-Condensation Kinetics of Different Silane Coupling Agents," *Phosphorus, Sulfur, and Silicon and the Related Elements*, vol. 186, no. 2, pp. 240–254, 2011.
- [14] L. Jinhua and Z. Guangyuan, "Polystyrene Microbeads by Dispersion Polymerization: Effect of Solvent on Particle Morphology," *International Journal of Polymer Science*, 2014.
- [15] C. K. Ober, K. P. Lok, and M. L. Hair, "Monodispersed, micron-sized polystyrene particles by dispersion polymerization," *Journal of Polymer Science: Polymer Letters Edition*, vol. 23, no. 2, pp. 103–108, 1985.
- [16] K.P. Lok, and C. K. Ober, "Particle size control in dispersion polymerization of polystyrene," *Canadian Journal of Chemistry*, vol. 63, no. 1, pp.209-216, 1985.
- [17] H. Qi, W. Hao, H. Xu, Z. Junying, and T. Wang, "Synthesis of large-sized monodisperse polystyrene microspheres by dispersion polymerization with dropwise monomer feeding procedure," *Colloid and Polymer Science*, vol. 287, pp. 243–248, 2009.
- [18] C. C. Liao, S. H. Wu, T. S. Su, M. L. Shyu, and C. M. Shu, "Thermokinetics evaluation and simulations for the polymerization of styrene in the presence of various inhibitor concentrations," *Journal of Thermal Analysis and Calorimetry*, vol. 85, no. 1, pp. 65–71, 2006.
- [19] M.F. Kemmere, M.J.J. Meuldijk, and A.A.H. Drinkenburg, "The influence of 4-tert-butylcatechol on the emulsion polymerization of styrene" *Journal of Applied Polymer Science*, vol. 71, no.14, pp. 2419-2422, 1999.
- [20] Y. Chen and H.-W. Yang, "Hydroxypropyl cellulose (HPC)-stabilized dispersion polymerization of styrene in polar solvents: Effect of reaction parameters," *Journal of Polymer Science Part A: Polymer Chemistry*, vol. 30, no. 13, pp. 2765–2772, 1992.
- [21] C. E. C. Jr, *Seymour/Carraher's Polymer Chemistry: Sixth Edition*. CRC Press, 2003.

- [22] C. Yu, D. Yang, F. Wu, and X. Shi, "Synthesis of PMMA/Polysiloxane Core-Shell Latex," *MATEC Web of Conferences*, vol. 25, p. 02004, 2015.
- [23] G. Hu, D. Yu, J. Zhang, H. Liang, and Z. Cao, "Synthesis of micron-sized poly(styrene-co-divinylbenzene) hollow particles from seeded emulsions by using swelling solvents," *Colloid J*, vol. 73, no. 4, pp. 557–564, 2011.
- [24] B. Liu, Y. Wang, M. Zhang, and H. Zhang, "Initiator Systems Effect on Particle Coagulation and Particle Size Distribution in One-Step Emulsion Polymerization of Styrene," *Polymers*, vol. 8, no. 2, p. 55, 2016.
- [25] A. Mahjub, "Monte Carlo simulation of the dispersion polymerization of styrene," *RSC Advances*, vol. 6, no. 54, pp. 48973-48984, 2016.
- [26] P. Šálek, D. Horák, and J. Hromádková, "Novel Preparation of Monodisperse Poly(styrene-co-divinylbenzene) Microspheres by Controlled Dispersion Polymerization," *Polymer Science, Series B*, vol. 60, no. 1, pp. 9–15, 2018.
- [27] X. Lu, and Z. Xin, "Synthesis of poly (styrene-co-3-trimethoxysilyl propyl methacrylate) microspheres coated with polysiloxane layer," *Colloid and Polymer Science*, vol. 285, no. 5, pp. 599-604, 2007.
- [28] D. Olmos, E. V. Martín, and J. González-Benito, "New molecular-scale information on polystyrene dynamics in PS and PS–BaTiO₃ composites from FTIR spectroscopy," *Phys. Chem. Chem. Phys.*, vol. 16, no. 44, pp. 24339–24349, 2014.
- [29] L. Durães, A. Maia, and A. Portugal, "Effect of additives on the properties of silica-based aerogels synthesized from methyltrimethoxysilane (MTMS)," *The Journal of Supercritical Fluids*, vol. 106, pp. 85–92, 2015.
- [30] V. Ozbolat, M. Dey, B. Ayan, A. Povilianskas, M. C. Demirel, and I. T. Ozbolat, "3D Printing of PDMS Improves Its Mechanical and Cell Adhesion Properties," *ACS Biomaterials Science & Engineering*, vol. 4, no. 2, pp. 682–693, Aug. 2018.
- [31] M. Zalaznik, M. Kalin, and S. Novak, "Influence of the processing temperature on the tribological and mechanical properties of poly-ether-ether-ketone (PEEK) polymer," *Tribology International*, vol. 94, pp. 92–97, 2016.

- [32] M. Vaezi and S. Yang, "Extrusion-based additive manufacturing of PEEK for biomedical applications," *Virtual and Physical Prototyping*, vol. 10, no. 3, pp. 123–135, Mar. 2015.
- [33] Y. Wang, W.-D. Müller, A. Rumjahn, and A. Schwitalla, "Parameters Influencing the Outcome of Additive Manufacturing of Tiny Medical Devices Based on PEEK," *Materials*, vol. 13, no. 2, p. 466, 2020.
- [34] W. Wu, P. Geng, G. Li, D. Zhao, H. Zhang, and J. Zhao, "Influence of Layer Thickness and Raster Angle on the Mechanical Properties of 3D-Printed PEEK and a Comparative Mechanical Study between PEEK and ABS," *Materials*, vol. 8, no. 9, pp. 5834–5846, 2015.
- [35] C. Yang, X. Tian, D. Li, Y. Cao, F. Zhao, and C. Shi, "Influence of thermal processing conditions in 3D printing on the crystallinity and mechanical properties of PEEK material," *Journal of Materials Processing Technology*, vol. 248, pp. 1–7, 2017.
- [36] S. Kumar, D. P. Anderson, and W. Adams, "Crystallization and morphology of poly(aryl-ether-ether-ketone)," *Polymer*, vol. 27, no. 3, pp. 329–336, 1986.
- [37] R. L. Blaine, "Determination of Polymer Crystallinity by DSC", TA Instruments, pp. 1-3 [Online].
- [38] J. Ho and T. R. Jow, "Effect of crystallinity and morphology on dielectric properties of PEEK at elevated temperature," *2013 IEEE International Conference on Solid Dielectrics (ICSD)*, pp. 385–388, 2013.
- [39] M. Yuan, J. A. Galloway, R.J. Hoffman, and S. Bhatt, "Influence of molecular weight on rheological, thermal, and mechanical properties of PEEK," *Polymer Engineering & Science*, vol. 51, no. 1, pp.94-102, 2011.
- [40] "Finishing Operations," *Finishing Operations*. Victrex plc , 2016.
- [41] "Dynamic Mechanical Analysis (DMA) A Beginner's Guide," *PerkinElmer*, p. 23, 2013.
- [42] K. P. Menard, and N. Menard, "Dynamic mechanical analysis," *Encyclopedia of Analytical Chemistry: Applications, Theory and Instrumentation*, pp. 1-25, 2006.
- [43] I. Narisawa and M. Ishikawa, "Crazing in semicrystalline thermoplastics," *Crazing in Polymers Vol. 2 Advances in Polymer Science*, pp. 353–391.

- [44] R. Kumar, M. Mamlouk, and K. Scott, "Sulfonated polyether ether ketone – sulfonated graphene oxide composite membranes for polymer electrolyte fuel cells," *RSC Adv.*, vol. 4, no. 2, pp. 617–623, 2014.
- [45] S. J. Lee, S. Mukerjee, J. McBreen, Y. W. Rho, and T. H. Lee, "Effects of Nafion impregnation on performances of PEMFC electrodes," *Electrochimica Acta*, vol. 43, no. 24, pp. 3693-3701, 1998.
- [46] S. D. Mikhailenko, W. Keping S. Kaliaguine, P. Xing, G. P. Robertson, and M. D. Guiver, "Proton conducting membranes based on cross-linked sulfonated poly (ether ether ketone)(SPEEK)," *Journal of Membrane Science*, vol. 233, no. 1-2, pp. 93-99, 2004.
- [47] P. Knauth, H. Hou, E. Bloch, E. Sgreccia, and M. L. Di Vona, "Thermogravimetric analysis of SPEEK membranes: thermal stability, degree of sulfonation and cross-linking reaction," *Journal of Analytical and Applied Pyrolysis*, vol. 92, no. 2, pp. 361-365, 2011.
- [48] K. Park et al., "Flexible Nanocomposite Generator Made of BaTiO₃ Nanoparticles and Graphitic Carbons," *Advanced Materials*, vol. 24, no. 22, pp. 2999-3004, 2012.
- [49] Z. Dang, S. Yao, J. Yuan and J. Bai, "Tailored Dielectric Properties based on Microstructure Change in BaTiO₃-Carbon Nanotube/Polyvinylidene Fluoride Three-Phase Nanocomposites," *The Journal of Physical Chemistry C*, vol. 114, no. 31, pp. 13204-13209, 2010.
- [50] Y. Jin, N. Xia and R. Gerhardt, "Enhanced dielectric properties of polymer matrix composites with BaTiO₃ and MWCNT hybrid fillers using simple phase separation," *Nano Energy*, vol. 30, pp. 407-416, 2016.
- [51] H. Kim, M. Shuvo, H. Karim, J. Noveron, T. Tseng and Y. Lin, "Synthesis and characterization of CeO₂ nanoparticles on porous carbon for Li-ion battery," *MRS Advances*, vol. 2, no. 54, pp. 3299-3307, 2017.
- [52] H. Kim et al., "Porous Carbon/CeO₂ Nanoparticles Hybrid Material for High-Capacity Super-Capacitors," *MRS Advances*, vol. 2, no. 46, pp. 2471-2480, 2017.
- [53] L. Cai, L. Song, P. Luan, Q. Zhang, N. Zhang, Q. Gao, D. Zhao, X. Zhang, M. Tu, F. Yang, W. Zhou, Q. Fan, J. Luo, W. Zhou, P. M. Ajayan, and S. Xie, "Super-stretchable,

- Transparent Carbon Nanotube-Based Capacitive Strain Sensors for Human Motion Detection,” *Scientific Reports*, vol. 3, no. 1, 2013.
- [54] D. J. Cohen, D. Mitra, K. Peterson, and M. M. Maharbiz, “A Highly Elastic, Capacitive Strain Gauge Based on Percolating Nanotube Networks,” *Nano Letters*, vol. 12, no. 4, pp. 1821–1825, 2012.
- [55] G. Georgousis, C. Pandis, A. Kalamiotis, P. Georgiopoulos, A. Kyritsis, E. Kontou, P. Pissis, M. Micusik, K. Czanikova, J. Kulicek, and M. Omastova, “Strain sensing in polymer/carbon nanotube composites by electrical resistance measurement,” *Composites Part B: Engineering*, vol. 68, pp. 162–169, 2015.
- [56] P. Dharap, Z. Li, S. Nagarajaiah, and E. V. Barrera, “Nanotube film based on single-wall carbon nanotubes for strain sensing,” *Nanotechnology*, vol. 15, no. 3, pp. 379–382, 2004.
- [57] T. Yamada, Y. Hayamizu, Y. Yamamoto, Y. Yomogida, A. Izadi-Najafabadi, D. N. Futaba, and K. Hata, “A stretchable carbon nanotube strain sensor for human-motion detection,” *Nature Nanotechnology*, vol. 6, no. 5, pp. 296–301, 2011.
- [58] K. Inpil, M.J. Schulz, J. Kim, V. Shanov, and D. Shi, "A carbon nanotube strain sensor for structural health monitoring," *Smart materials and structures*, vol. 15, no. 3, pp.737, 2006.
- [59] D. Chung, “Self-monitoring structural materials,” *Materials Science and Engineering: R: Reports*, vol. 22, no. 2, pp. 57–78, 1998.
- [60] H. Kim, T. Fernando, M. Li, Y. Lin, and T.-L. B. Tseng, “Fabrication and characterization of 3D printed BaTiO₃/PVDF nanocomposites,” *Journal of Composite Materials*, vol. 52, no. 2, pp. 197–206, 2017.
- [61] H. Kim, F. Torres, Y. Wu, D. Villagran, Y. Lin, and T.-L. B. Tseng, “Integrated 3D printing and corona poling process of PVDF piezoelectric films for pressure sensor application,” *Smart Materials and Structures*, vol. 26, no. 8, p. 085027, 2017.
- [62] H. Kim, F. Torres, D. Villagran, C. Stewart, Y. Lin, and T.-L. B. Tseng, “3D Printing of BaTiO₃/PVDF Composites with Electric In Situ Poling for Pressure Sensor Applications,” *Macromolecular Materials and Engineering*, vol. 302, no. 11, p. 1700229, 2017.

- [63] H. Kim, F. Torres, T. Islam, D. Islam, L. A. Chavez, C. A. G. Rosales, B. R. Wilburn, C. M. Stewart, J. C. Noveron, T.-L. B. Tseng, and Y. Lin, “Increased piezoelectric response in functional nanocomposites through multiwall carbon nanotube interface and fused-deposition modeling three-dimensional printing – CORRIGENDUM,” *MRS Communications*, vol. 7, no. 4, pp. 974–974, 2017.
- [64] H. Kim, J. Johnson, L. A. Chavez, C. A. G. Rosales, T.-L. B. Tseng, and Y. Lin, “Enhanced dielectric properties of three phase dielectric MWCNTs/BaTiO₃/PVDF nanocomposites for energy storage using fused deposition modeling 3D printing,” *Ceramics International*, vol. 44, no. 8, pp. 9037–9044, 2018.
- [65] Z.-M. Dang, S.-H. Yao, and H.-P. Xu, “Effect of tensile strain on morphology and dielectric property in nanotube/polymer nanocomposites,” *Applied Physics Letters*, vol. 90, no. 1, p. 012907, 2007.
- [66] F. A. Sanchez and J. González-Benito, “PVDFBaTiO₃/carbon nanotubes ternary nanocomposites: Effect of nanofillers and processing,” *Polymer Composites*, vol. 38, no. 2, pp. 227–235, 2015.
- [67] X.-M. Meng, X.-J. Zhang, C. Lu, Y.-F. Pan, and G.-S. Wang, “Enhanced absorbing properties of three-phase composites based on a thermoplastic-ceramic matrix (BaTiO₃ PVDF) and carbon black nanoparticles,” *J. Mater. Chem. A*, vol. 2, no. 44, pp. 18725–18730, 2014.
- [68] T. Zhou, J.-W. Zha, R.-Y. Cui, B.-H. Fan, J.-K. Yuan, and Z.-M. Dang, “Improving Dielectric Properties of BaTiO₃/Ferroelectric Polymer Composites by Employing Surface Hydroxylated BaTiO₃ Nanoparticles,” *ACS Applied Materials & Interfaces*, vol. 3, no. 7, pp. 2184–2188, Oct. 2011.
- [69] V. Petrovsky, T. Petrovsky, S. Kamlapurkar, and F. Dogan, “Dielectric Constant of Barium Titanate Powders Near Curie Temperature,” *Journal of the American Ceramic Society*, vol. 91, no. 11, pp. 3590–3592, 2008.
- [70] Z.-M. Dang, Y.-Q. Lin, H.-P. Xu, C.-Y. Shi, S.-T. Li, and J. Bai, “Fabrication and Dielectric Characterization of Advanced BaTiO₃/Polyimide Nanocomposite Films with High

- Thermal Stability,” *Advanced Functional Materials*, vol. 18, no. 10, pp. 1509–1517, May 2008.
- [71] J. W. Liou and B. S. Chiou, “Dielectric tunability of barium strontium titanate/silicone-rubber composite,” *Journal of Physics: Condensed Matter*, vol. 10, no. 12, pp. 2773–2786, 1998.
- [72] B. Lee and K. Auh, “Effect of grain size and mechanical processing on the dielectric properties of BaTiO₃,” *Journal of Materials Research*, vol. 10, no. 6, pp. 1418–1423, 1995.
- [73] C. M. Dhar and P. K. C. Pillai, “Thermocompensated capacitor with barium titanate (BaTiO₃)/polyvinylidene fluoride (PVDF) composite,” *Journal of Materials Science Letters*, vol. 6, no. 1, pp. 33–34, 1987.
- [74] C. Muralidhar and P. K. C. Pillai, “Dielectric behaviour of barium titanate (BaTiO₃)/polyvinylidene fluoride (PVDF) composite,” *Journal of Materials Science Letters*, vol. 6, no. 3, pp. 346–348, 1987.
- [75] T. Tsurumi, K. Soejima, T. Kamiya, and M. Daimon, “Mechanism of Diffuse Phase Transition in Relaxor Ferroelectrics,” *Japanese Journal of Applied Physics*, vol. 33, no. Part 1, No. 4A, pp. 1959–1964, 1994.
- [76] B. Lee and K. Auh, “Effect of grain size and mechanical processing on the dielectric properties of BaTiO₃,” *Journal of Materials Research*, vol. 10, no. 6, pp. 1418–1423, 1995.
- [77] Z.-M. Dang, M.-S. Zheng, and J.-W. Zha, “1D/2D Carbon Nanomaterial-Polymer Dielectric Composites with High Permittivity for Power Energy Storage Applications,” *Small*, vol. 12, no. 13, pp. 1688–1701, Nov. 2016.
- [78] M.-Y. Shen, T.-Y. Chang, T.-H. Hsieh, Y.-L. Li, C.-L. Chiang, H. Yang, and M.-C. Yip, “Mechanical Properties and Tensile Fatigue of Graphene Nanoplatelets Reinforced Polymer Nanocomposites,” *Journal of Nanomaterials*, vol. 2013, pp. 1–9, 2013.
- [79] D. Bikiaris, “Microstructure and Properties of Polypropylene/Carbon Nanotube Nanocomposites,” *Materials*, vol. 3, no. 4, pp. 2884–2946, 2010.

- [80] Y. Zhou, F. Pervin, L. Lewis, and S. Jeelani, "Experimental study on the thermal and mechanical properties of multi-walled carbon nanotube-reinforced epoxy," *Materials Science and Engineering: A*, vol. 452-453, pp. 657–664, 2007.
- [81] Y. Zhou, F. Pervin, L. Lewis, and S. Jeelani, "Fabrication and characterization of carbon/epoxy composites mixed with multi-walled carbon nanotubes," *Materials Science and Engineering: A*, vol. 475, no. 1-2, pp. 157–165, 2008.
- [82] Y.-K. Choi, K.-I. Sugimoto, S.-M. Song, Y. Gotoh, Y. Ohkoshi, and M. Endo, "Mechanical and physical properties of epoxy composites reinforced by vapor grown carbon nanofibers," *Carbon*, vol. 43, no. 10, pp. 2199–2208, 2005.

Vita

Bethany R. Wilburn was born in El Paso, Texas in April 1996. Ms. Wilburn completed her Bachelor of Science in Mechanical Engineering at The University of Texas at El Paso in December 2018. At the end of her junior year, Ms. Wilburn began working as an undergraduate research assistant working with Dr. Yirong Lin under the NSF Partnership for Research and Education in Materials Research (NSF-PREM) program. In January 2019, she continued her graduate studies at The University of Texas at El Paso pursuing a master's degree in Mechanical Engineering under the supervision of Dr. Yirong Lin. Her research focused on leading a collaborative research project with Kansas City National Security Campus (KCNSC) for the development of polysiloxane microspheres as pore formers for additive manufacturing. Over the past four years, Ms. Wilburn has co-authored in 6 journal publications due to her research efforts.

Contact Information (Email): wilburnbethany2107@gmail.com